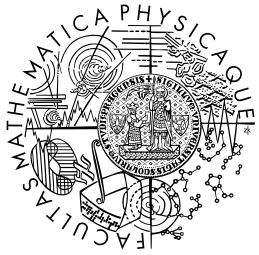

FACULTY
OF MATHEMATICS
AND PHYSICS
Charles University

MASTER THESIS

Bc. Andrej Farkaš

Investigation of effects of femtosecond laser pulses on spintronic structures

Department of Chemical Physics and Optics

Supervisor of the master thesis: Mgr. Kamil Olejník, Ph.D.
Study programme: Physics
Study branch: Optoelectronics and photonics

Prague 2021

I declare that I carried out this master thesis independently, and only with the cited sources, literature and other professional sources. It has not been used to obtain another or the same degree.

I understand that my work relates to the rights and obligations under the Act No. 121/2000 Sb., the Copyright Act, as amended, in particular the fact that the Charles University has the right to conclude a license agreement on the use of this work as a school work pursuant to Section 60 subsection 1 of the Copyright Act.

In ..... date ....

Author's signature

This thesis focuses on my work in the group of prof. Tomáš Jungwirth at the FZÚ, AV ČR in Prague and at the laboratories of the MFF UK in Prague. I have done all of the presented work during my master's studies between the years 2019 and 2021.

I want to thank my supervisor Kamil Olejník for his guidance and friendship in the past years. He offered me advice whenever I needed one and gave me a lot of insight into the context of my work.

Many thanks also belong to prof. Tomáš Jungwirth as a leader of this group, but also as a brilliant theoretician, for building up the theory that allowed this work along with Jakub Železný, Karel Výborný and others.

This work would also not be possible without Vít Novák and Filip Křížek, who were responsible for the growth of CuMnAs. I would also like to thank my colleague Jan Zubáč for his experimental insights, and technicians Zbyněk Šobáň, Karel Hruška, Vlastimil Jurka, and Jiří Zyka took care of the equipment needed for the manufacturing of samples.

Special thanks also go to my colleague and friend Zdeněk Kašpar, who paved the way for my optical experiment with his rigorous electrical measurements.

Since an important part of this work was conducted at Charles University, I would like to thank prof. Petr Němec as the head of the department where it was conducted. I am also thankful to my colleague and friend Miloš Surýnek, who took care of the optical setup, helped me get everything up and running, and was my frequent consultant with everything regarding the optical measurements.

Lastly, I would like to thank my family and friends for their continuous support during many different problems I encountered.

Title: Investigation of effects of femtosecond laser pulses on spintronic structures

Author: Bc. Andrej Farkaš

Department: Department of Chemical Physics and Optics

Supervisor: Mgr. Kamil Olejník, Ph.D., Fyzikální ústav AV ČR, v. v. i.

Abstract: This thesis is focused on a detailed investigation of the optically induced quench switching effect in different films of antiferromagnetic CuMnAs. The quench switching effect was recently discovered to be highly reproducible resistance switching, which can be excited by electrical and optical laser pulses. This thesis compares the amplitude response to laser-induced quench switching for samples on the different substrate material, samples with different stoichiometries, and samples with different thicknesses of CuMnAs film. The effects of different ratios between the laser spot and the size of the measured device are investigated, and position-dependent measurements are also presented. It is shown that resistivity change with optical excitation using a single 120 femtosecond laser pulse can, in ideal conditions, reach up to 15% at room temperature, which is comparable with the maximum signal obtained with electrical pulses. All of the measurements combined with current knowledge of quench switching illustrate the robust behavior of this mechanism across a wide range of conditions.

Keywords: Antiferromagnetic spintronics CuMnAs Optical excitation Quench switching Femtosecond laser pulses

Contents

Introduction

Recently, a new Quench switching effect was discovered in thin films of antiferromagnetic tetragonal CuMnAs [1]. This effect is characterized by large resistivity changes reaching 20% at room temperature and 100% at low temperatures making it comparable to the GMR effect. A comprehensive study of this effect was done using strong electrical current pulses [2]. Initial experiments also demonstrated the possibility of optically induced quench switching using femtosecond laser pulses.

The aim of this thesis is the detailed investigation of quench switching using optical excitation. Previous work demonstrating the optically induced quench switching was conducted using a small laser spot, which required a train of femtosecond pulses to induce a measurable quench switching signal. In this work, we use a large laser spot, which allows the excitation of a significant part of the measured device. The need for a larger laser spot prompted the building of a new optical setup, constructed with some help from the author. This new setup allowed a single 120 femtosecond laser pulse excitation with an electrical readout of the device. The single-pulse excitation with increasing laser intensity (fluence) was the method we chose for the investigation of quench switching behavior for various CuMnAs films.

First, the response of the 50 nm CuMnAs films grown on different substrates will be presented. 50 nm films are characterized by their layer quality with good homogeneity and a low number of structural defects; therefore, they are usually used as a reference [3]. The CuMnAs films grown on a GaP substrate show the most consistent quality. Therefore CuMnAs films on GaP were selected to investigate differences in quench switching for by different stoichiometries. Another evaluated aspect of CuMnAs films was their thicknesses. Lastly, the role of the ratio between the laser spot and the device size will also be evaluated.

The quench switching critically depends on the temperature. It occurs when the local temperature exceeds the Neél temperature; therefore, only a portion of a Gaussian laser spot is causing the quench switching. The positional measurements were used to determine the actual writing region of the laser spot. Another motivation for positional measurements was to evaluate the sensitivity to the laser spot location on the device. This sensitivity was explored in the mapping experiment, which shows the quench switching amplitude dependence on the laser spot position. Numerical simulations also accompanied this mapping experiment to evaluate its results.

1. Theorethical knowledge of antiferromagnetic spintronics

The first chapter of this thesis is dedicated to the theoretical knowledge of the studied field.

It starts with the description of the magnetic properties of solids. It details types of magnetic materials with a focus on ferromagnetic and antiferromagnetic materials and their internal structure.

The second section is dedicated to the magnetoresistance effects in the presence of the magnetic field. Anisotropic magnetoresistance and giant magnetoresistance will be explained in more detail.

From the third section onwards, the focus of this section shifts toward the antiferromagnetic material CuMnAs. In the fourth section, electrical switching using Neél vector reorientation is described.

In the fifth section, the newly discovered quench switching in CuMnAs is explored.

Lastly, in the sixth section, the interaction between the laser light and thin films of CuMnAs is described.

1.1 Magnetic properties of materials

1.1.1 Magnetism

All materials exhibit some type of magnetic behavior depending on their elementary composition and atomic structure.

In the next part of this section magnetic properties of a single atom will be described and how these single atoms interact in different types of magnetic ordering. Ferromagnetism and antiferromagnetism will be in focus because of their relevance to the topic of this thesis. Other types of magnetism are going to be mentioned as well.

1.1.2 Magnetic properties of a single atom

The magnetic properties of a single atom are given by its electron configuration. For atom in a ground state, this configuration is determined by the usage of empirical Hund's rules [4]. These rules were formulated in 1927 by German physicist Friedrich Hund.

The first rule states that the term with maximum multiplicity has the lowest energy stemming from Pauli's exclusion principle for a given electron configuration. Multiplicity is equal to **2S+1**, where **S** is total spin angular momentum. As a result term with the lowest energy is the one with the highest total spin number **S**, which is calculated as a sum of electrons spin $m_s = 1/2$ or $m_s = -1/2$. Value for an individual electron is dependent on chosen direction z.

The second rule states that for a given multiplicity, the term with the most significant value of total orbital angular momentum number **L** has the lowest energy. This formulation reflects the Coulomb interaction between the electrons.

Finally, the third rule states that for a given term in an atom with an outermost shell half-filled or less, the level with the lowest total angular momentum **J** has the lowest energy. In case when the outermost shell is more than half-filled, the level with the highest value of **J** has the lowest energy. $J = L + S$ This rule reflects spin-orbit interaction.

Knowing these rules magnetic moment of an atom can be calculated using the equation:

$$\mu = -g\mu_B J \tag{1.1}$$

where the μ_B is the Bohr magneton, and g is the Landé g-factor. As a result of these rules, atoms with partially filled orbitals show non-zero magnetic moment. An example of this is shown in figure 1.1 for elements of 3d group.

If atoms are kept close together, like in a crystal structure, a local environment they create must be considered. Due to the interaction of neighboring atoms, their orbitals deform. This mandates a correction that is significant in the d-orbitals, as they are far from the nucleus. Because of this correction, the total momentum of 3d elements is given mostly by their spin momentum (as $L \to 0$).

1.1.3 Magnetic structure

Magnetic atoms in solids interact by exchange interactions. Their type and strength determine the magnetic ground state of the system. The basic tree

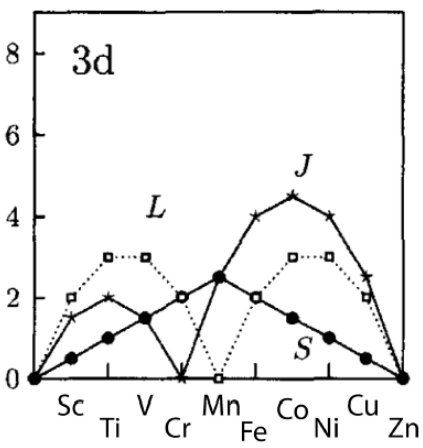

Figure 1.1: S, L and J for 3d atoms according to Hund's rules. Adapted from [4].

structure of magnetic properties in solids is shown in figure 1.2. In this subsection, only a basic overview of different types of magnetic ordering is provided. A more detailed description of ferromagnetic and antiferromagnetic properties will be given in the next subsection.

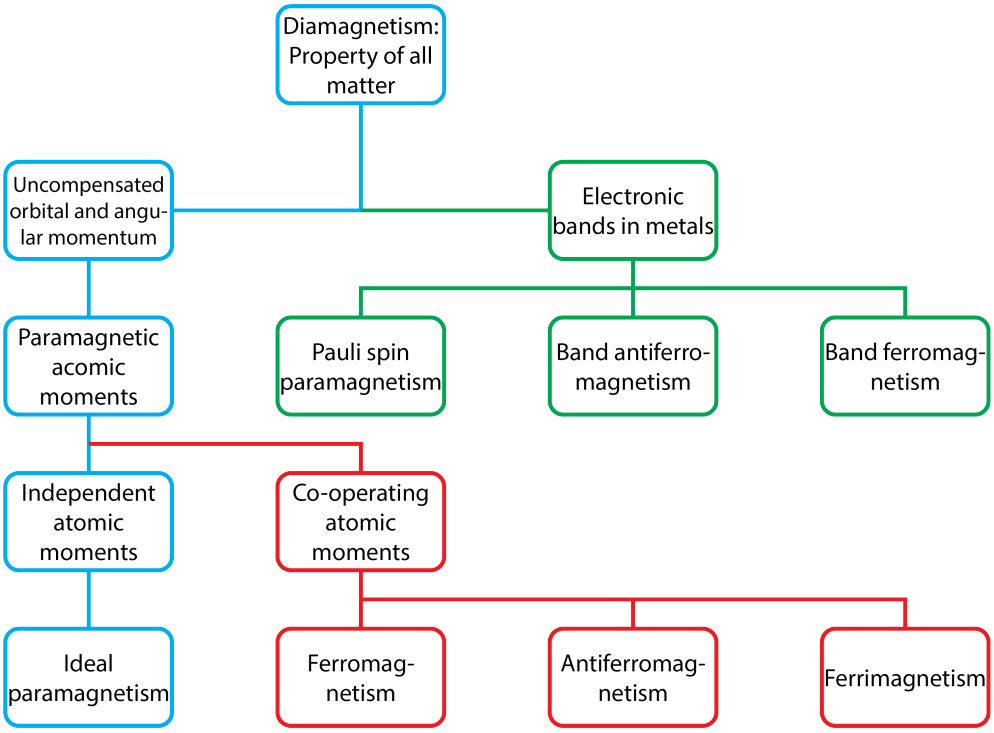

Figure 1.2: The family tree of magnetism. Adapted from [5].

Diamagnetism is the inherent property of all materials, and it is a tendency to oppose applied magnetic field. Due to the weak nature of this effect, it is detectable only in purely diamagnetic materials.

Paramagnetism occurs in materials with unpaired electrons, e.g., one electron in atomic/molecular orbital. Since Pauli's exclusion principle does not bind

these electrons, their magnetic moments are free to align with the direction of an external magnetic field, which results in its reinforcement.

Ferromagnetism can be found in materials with unpaired electrons. The moments of atoms in ferromagnet spontaneously align in parallel directions due to mutual exchange interactions resulting in spontaneous net magnetic moment formation. Upon application of the external magnetic field, the moments of ferromagnet align in its direction.

Antiferromagnetism, unlike ferromagnetism, is characterized by the tendency of magnetic moments to align antiparallel for neighboring atoms. Due to this effect, antiferromagnets exhibit zero net magnetic moment.

Ferrimagnetism can be described as a combination of ferromagnetism and antiferromagnetism. Like antiferromagnetism, neighboring atoms have antiparallel magnetic moments, but they exhibit unequal magnitude. Due to this inequality, ferrimagnetic materials exhibit non-zero net magnetic moment and emit a magnetic field.

1.1.4 Ferromagnetism and antiferromagnetism

As mentioned before, ferromagnetic materials have all magnetic moments ordered in a parallel orientation, while antiferromagnets have an antiparallel orientation of neighboring magnetic moments. Both configurations are shown in figure 1.3.

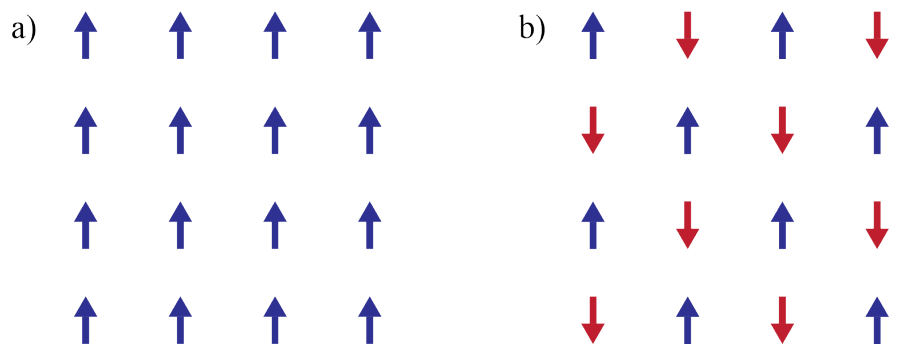

Figure 1.3: a) Ferromagnetic and b) collinear antifferomagnetic configuration.

The ground state alignment of magnetic moments is, in both cases, a solution of the Heisenberg's model

$$\hat{H} = -\sum_{(i,j)} J_{ij}\mathbf{S}_i \cdot \mathbf{S}_j + g\mu_B \sum_j \mathbf{S}_j \cdot \mathbf{B} \tag{1.2}$$

where the first term represents spin-spin interaction and the second term represents interaction with external magnetic field $\mathbf{B}$ (Zeeman energy). The exchange constant J_{ij} is a quantification of an exchange interaction between i^{th} and j^{th} atom with their respective spin momentum $\mathbf{S}_i$ and $\mathbf{S}_j$.

This model can be simplified using Wiess molecular field [6]. This field $\mathbf{B}_{mf}$ represents an effective molecular field. This effective molecular field is then combined with the external magnetic field. That, in turn, reduces the Heisenberg model hamiltonian into simplified form [4].

$$\hat{H} = g\mu_B \sum_j \mathbf{S}_j \cdot (\mathbf{B} + \mathbf{B}_{mf}) \tag{1.3}$$

This equation takes similar form as the Zeeman energy in previous equation, but the magnetic field is replaced by the effective magnetic field $\mathbf{B}+\mathbf{B}_{mf}$. Molecular field is proportional to the magnetization $\mathbf{M}$ in this model

$$\mathbf{B}_{mf} = \lambda \mathbf{M} \tag{1.4}$$

where λ represents effects of all the exchange constants J_{ij} on one atom.

For ferromagnetic materials is the Weiss effective field parameter $\lambda > 0$. This represents a case where positive exchange interaction is dominant. Parallel ground state configuration is a result of this dominance and is shown in figure 1.3a.

The solution of the Weiss model is temperature-dependent magnetization $\mathbf{M}$. It encompasses exchange interactions with rising thermal fluctuations. As a result of a combination of these competing effects, the critical temperature is introduced. In ferromagnets, it is called Curie temperature T_C. With the rising temperature, the magnetization decreases from a saturated value of M_S in zero-temperature limit. After reaching the Curie temperature, the magnetization is zero, and the material becomes paramagnetic.

In contrast with the ferromagnets, in the antiferromagnets, dominant exchange constant J_{ij} is negative, thus parameter $\lambda < 0$. This favors the antiparallel ground configuration shown in figure 1.3b. In this figure, collinear antiferromagnet is depicted. In this configuration, antiferromagnetic order stems from two antiparallel moments with the same amplitude. Due to this configuration, collinear antiferromagnetic crystals can be interpreted as two sublattices with the parallel alignment of magnetic moments. Example is shown in figure 1.4. In other non-collinear configurations condition of the net-zero magnetic moment has to be fulfilled for each elementary cell.

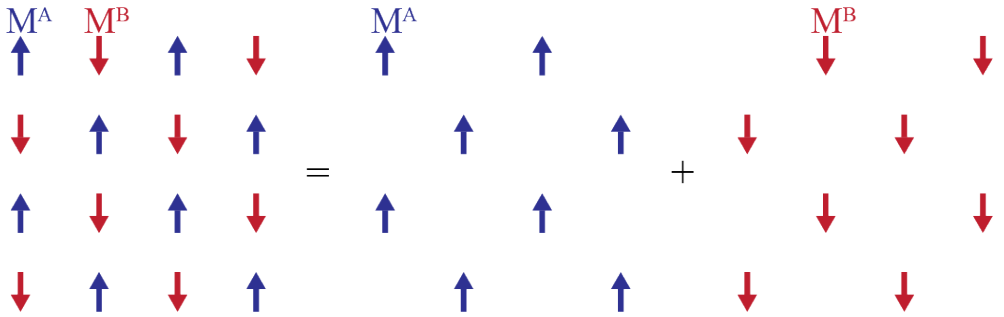

Figure 1.4: Two opposing sublatticies of an antiferromagnet.

Molecular field is different for each sublattice

$$\begin{aligned} \mathbf{B}^A_{mf} &= -|\lambda|\,\mathbf{M}^B \\ \mathbf{B}^B_{mf} &= -|\lambda|\,\mathbf{M}^A \end{aligned} \tag{1.5}$$

The solution of this model is very similar to the ferromagnets because the two magnetization vectors have the same amplitude but opposite direction $\mathbf{M}^A = -\mathbf{M}^B$. The critical temperature, which marks the transition from antiferromagnetic to paramagnetic state, is called the Néel temperature T_N. Below this temperature, both sublattices have non-zero net magnetization.

1.1.5 Magnetic domain structure

Magnetic domains are typically present in magnetically ordered materials [7]. Separated by domain walls, they create regions with different orientations of the magnetic order. The width of the domain walls is dependent on the ratio between the exchange interaction and the magnetic anisotropy of the system.

In ferromagnets, the domain structure is affected by the long-range dipole interaction. Its first effect is fast growth (e.g., following domain nucleation while cooling below the Curie temperature from the paramagnetic state). The second effect is formation domain structure in macroscopic samples lowering total energy [8].

The lack of dipole magnetic field in antiferromagnets results in slower growth of domains, which is important for the quench switching effect studied in this work and is described in section 1.5.

In contrast, the antiferromagnets do not exhibit a dipole field during the transition from paramagnetic to antiferromagnetic state. This lack of an internal dipole field leads to the creation of a complex domain structure. Because of each domain's zero net magnetic moment, structural defects are the basis for the domain walls, and their width follows the same principles as in ferromagnets.

I the case of ferromagnets, the magnetization vector M is describing the domain orientation. In the case of antiferromagnets, the Neel vector $\mathbf{L}$ is used, which is defined as a difference of sublattice magnetizations:

$$\mathbf{L} = \mathbf{M}^A - \mathbf{M}^B \tag{1.6}$$

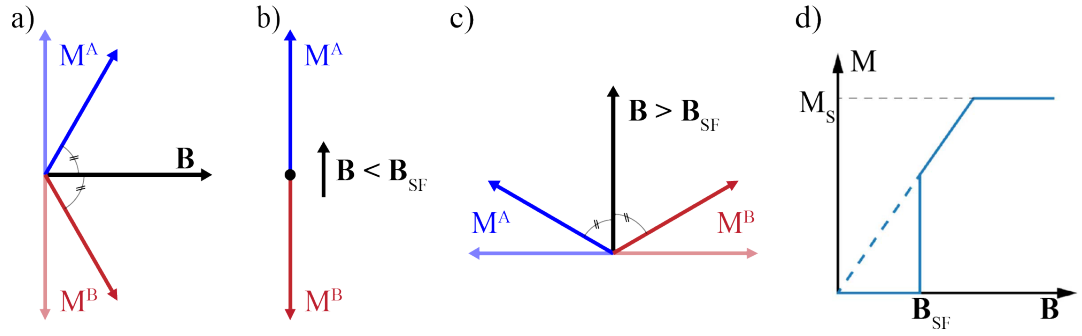

Figure 1.5: Antiferromagnets in the presence of an external magnetic field. a) When the field is applied perpendicular to the L vector, the magnetization will cant. b) External field has no effect when it is applied along the Néel vector, and its amplitude is below spin-flop field $\mathbf{B}_{SF}$. c) Spin-flop to the more energetically favorable configuration of magnetic moments perpendicular to the field and immediate canting. d) Macroscopic magnetization as a function of external field amplitude for B perpendicular to L (dashed line) and B parallel to L (solid line). Magnetization saturates when both sublattices are along the external field.

Antiferromagnets, like ferromagnets, exhibit anisotropy in their magnetic susceptibility, and thus their magnetization sublattices are naturally oriented in their easy axis. If then placed in an external magnetic field, antiferromagnets react depending on the angle between the Néel vector $\mathbf{L}$ and the $\mathbf{B}_{ext}$. If they are perpendicular to each other magnetic moments of both sublattices will cant towards the direction of $\mathbf{B}_{ext}$, as shown in figure 1.5a. When the direction of $\mathbf{B}_{ext}$

is parallel or antiparallel to Néel vector $\mathbf{L}$ no effect is observed (figure 1.5b) until $\mathbf{B}_{ext}$ reaches so-called spin-flop field $\mathbf{B}_{SF}$. For fields higher than the spin-flop field, magnetic moments of sublattices will align themselves perpendicularly to the external field and immediately cant towards it, as shown in figure 1.5c. The effect of canting further increases until the saturated value of $\mathbf{M}_S$ is reached. In the case of CuMnAs thin films value of $\mathbf{B}_{SF}$ is close to 2T was measured with magnetotransport, and XMLD-PEEM [9].

1.2 Magnetoresistance

Magnetoresistance is a general term for any resistivity change occurring in the presence of any magnetic interaction, whether that is the external magnetic field, internal magnetic moments, or others. Multiple types of magnetoresistance can be observed depending on a type of material, its composition, and its arrangement. Namely, geometrical magnetoresistance, negative magnetoresistance, anisotropic magnetoresistance (AMR), giant magnetoresistance (GMR), tunneling magnetoresistance (TMR), colossal magnetoresistance (CMR), and extraordinary magnetoresistance (EMR) can be observed. In the following paragraphs, AMR and GMR will be explored in detail.

1.2.1 Anisotropic magnetoresistance

Ferromagnetic materials exhibit a distinctive effect of change in resistivity depending on the angle between the magnetization and electric current direction called anisotropic magnetoresistance (AMR). The magnitude of the AMR is given by [10]

$$AMR = \frac{\Delta\rho}{\rho_{av}} = \frac{\rho_{\parallel} - \rho_{\perp}}{\frac{1}{3}\rho_{\parallel} + \frac{2}{3}\rho_{\perp}} \tag{1.7}$$

where $\rho_{\perp}$ is resistivity in the direction parallel to the current direction and $\rho_{\perp}$ in the perpendicular direction, equation 1.7 represents resistance change normalized by the average resistivity ρ_{av}.

The AMR in ferromagnets originates from the spin-orbit interaction and band splitting. For 3d transition metal alloys, s-d scattering probability is most significant for the electrons traveling parallel with the magnetization, therefore resulting in $\rho_{\parallel} > \rho_{\perp}$ [11].

This effect can be measured both in the current direction giving longitudinal resistivity ρ_{xx} or in the perpendicular direction giving transverse resistivity ρ_{xy}. The following formulae give the angular dependence of these resistivities

$$\begin{aligned} \rho_{xx} &\sim \cos 2\theta \\ \rho_{xy} &\sim \sin 2\theta \end{aligned} \tag{1.8}$$

AMR magnitudes are typically in the order of tenths of a percent. In the case of the CuMnAs thin films, the amplitudes are between 0.1-0.2% depending on the film thickness [12].

1.2.2 Giant magnetoresistance

The giant magnetoresistance (GMR) was first observed in 1988 [13] on heterostructures comprised of ferromagnetic layers which are separated by a thin non/magnetic film. Thanks to its much higher amplitudes compared with other magnetoresistance effects, the name giant was used.

The behavior of the resistivity is shown in figure 1.6a. With no external field applied (B=0), two neighboring ferromagnetic layers have antiparallel alignment (as shown in fig. 1.6b). With increasing external field, the resistance decreases until it saturates, corresponding to parallel alignment of neighboring magnetic layers.

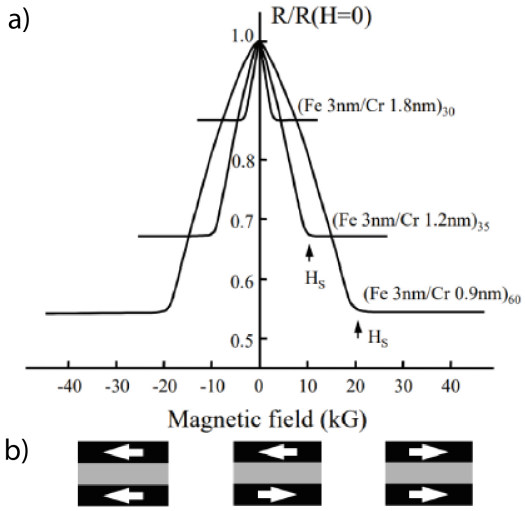

Figure 1.6: Giant magnetoresistance. a) Experimental observation of GMR in Fe/CR superlattices with different spacer thicknesses [13]. b) Schematic representation of orientations of the magnetic films. Adapted from [2]

As shown in figure 1.6a, the saturation level is strongly dependent on the spacer thickness. In the first measurement of the GMR [13] on superlattice Fe3nm/Cr0.9nm, the amplitude reached up to 80% at the temperature of 4K. With a reduction of the chromium layer thickness, amplitudes up to 220% were reached at 1.5K, and 42% at 300K [14]. In the case of different compositions of the superlattices like Co/Cu, the amplitude reaches 70% at 300K. When cobalt film is doped with iron, a record-holding superlattice is created with the GMR amplitude of 110% at 300K [15].

It is important to note that the GMR effect can be observed in two geometries. Standardly, the electrical current is applied perpendicular to the multilayer's surface (also perpendicular to the individual planes). However, the effect can also be observed for current applied in the planar direction, where it flows along with the interfaces. Measured amplitude in this geometry is smaller [16] but makes device fabrication easier. That makes it useful for industrial applications.

The two-current model proposed by Mott [17] can also be used to describe the GMR effect.

Two-current model

As proposed by Mott, the total conductivity of electrons σ can be expressed as [17]

$$\sigma = \sigma_{\downarrow} + \sigma_{\uparrow} \tag{1.9}$$

where the conductivities $\sigma_{\downarrow}$ and $\sigma_{\uparrow}$ correspond to down and up spin states. In magnetic materials, those conductivities can differ due to spin dependent density of states.

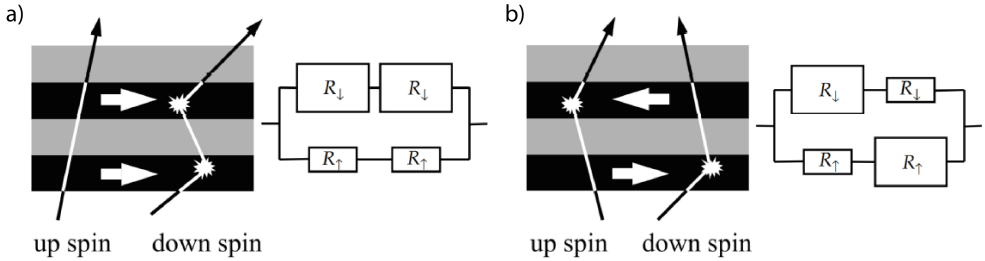

Figure 1.7: Two-current model of GMR. a) Representation of the parallel configuration of layers. The up-spin electrons have higher conductivity (smaller resistivity) in the ferromagnetic films. On the other hand the down-spin electrons have smaller conductivity. Equivalent resistor circuit is shown on the right. b) Antiparallel configuration of the ferromagnetic layers, which results in similar conductivities for both branches [18]. Adapted from [2]

Figure 1.7 shows the origin of GMR schematically expressing paths for electrons with spin up or down, respectively. This figure shows two currents, one for the up-spin electron and one for the down-spin electrons. In the parallel configuration of the ferromagnetic layers (with applied magnetic field), the up-spin electrons have larger conductivity in both layers. The down-spin electrons have low conductivity in both layers. This is represented with an equivalent resistor circuit in figure 1.7a, where two small resistors represent the up-spin branch while the down-spin branch has two large resistors. Thus, the current is dominated by up-spin electrons with their low resistance branch.

In figure 1.7b with antiparallel configuration (absence of external magnetic field), each electron branch experiences both high and low conductivity ergo circuit consists of both small and high resistor in each branch. This results in higher resistance in total compared to the parallel configuration.

If an insulating layer replaces the non-magnetic spacer, the GMR amplitude can be further increased. In that configuration, electrons have to tunnel between the magnetic layers, and the resulting change in the resistance is called the tunneling magnetoresistance (TMR) [19][20].

1.3 CuMnAs

CuMnAs is a high-temperature antiferromagnetic material. Its tetragonal phase is compatible with common semiconductor substrates such as GaP, Si, or GaAs and, therefore, can be grown using Molecular Beam Epitaxy (MBE). CuMnAs is a part of a family of collinear antiferromagnets along with Mn_2Au. CuMnAs also has noncentrosymmetric spin sublattices. Its crystalline structure with the magnetic moments of both Mn sublattices can be found in figure 1.8a and matching of CuMnAs onto GaP substrate is shown in figure 1.8b.

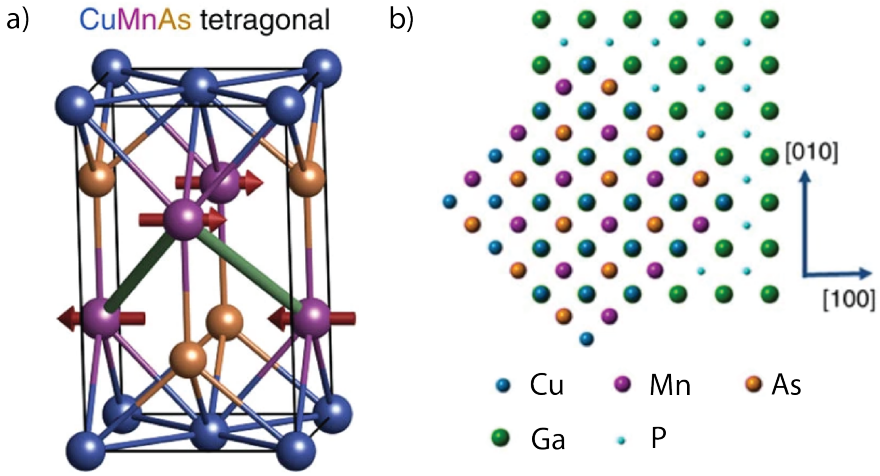

Figure 1.8: a) Crystallographic structure of orthorombic CuMnAs. Magnetic moments of Mn atoms are represented with arrows and they show two sublatticies with opposing magnetizations. b) Lattice matching on GaP substrate. Adapted from [21]

1.4 Néel vector switching in CuMnAs

This section will start historical overview of switching effects studied on CuMnAs. This should provide the reader with an insight into the effects present in thin CuMnAs films.

1.4.1 Torque in antiferromagnets

In any magnetic material with the presence of spin-polarized current new torques on the magnetic moments are created. These torques are usually small and do not influence the magnetization amplitude, but they can change the magnetization direction. The spin torques can be formulated with this equation [22]

$$\mathbf{T} \approx a_j \mathbf{M} \times (\mathbf{M} \times \mathbf{p}) + b_j \mathbf{M} \times \mathbf{p} \tag{1.10}$$

where vector $\mathbf{M}$ is magnetization and the vector $\mathbf{p}$ represents spin polarization. The first term of this equation ($\mathbf{M} \times (\mathbf{M} \times \mathbf{p})$) is called antidamping-like torque T_{AD}. The torque points in the direction of the polarization and causes tilting of the magnetization. The second term ($\mathbf{M} \times \mathbf{p}$) represents a field-like torque

T_{FL}. This torque causes precession of the magnetization similarly to the external magnetic field, which explains the name.

In the collinear antiferromagnets, these torques exhibit different behavior due to the two sub-lattices with opposite magnetizations.

The antidamping-like torque creates the torques in opposite directions for each of the two antiparallel sublattices. As a result, both magnetization vectors M_A and M_B will rotate in the same direction. However, the final state of this rotation is not deterministic and strongly depends on the excitation parameters. This stems from instability of the effective field, which changes with change in the magnetization [23].

The field-like torque acts on both magnetic moments in the same direction. This effect results in canting of the magnetization. To achieve any noticeable canting strong magnetic fields are required because of the strong exchange interaction between the two opposing moments.

A particular case of the field-like torque is the Néel spin-orbit torque (or staggered). In this configuration, the effective field direction alternates with the position of the atoms in the lattice. It can be observed only in materials with specific symmetry. These materials have to have lattice divisible into two sub-lattices which form inversion partners, with each of them having broken inversion symmetry. Because of that, each sub-lattice experiences an opposite electric field, and spin polarization induced by electrical current is also opposite. This results in a rotation of the opposite magnetic moments. When the rotation stops, both moments are perpendicular to the current direction.

1.4.2 Néel spin-orbit torque switching in CuMnAs

Thin CuMnAs films were the first material on which electrical switching induced by the Néel spin-orbit torque was measured [24]. A star-like device was used in the first measurements. This allowed varying the current pulse direction by 90° while also recording longitudinal and transverse resistivity signals after the pulse. This switching is shown in figure 1.9 for two configurations differing in their readout current direction. Enhancements in this switching technique allowed to reproduce these results for pulses in the sub-nanosecond region [25].

One characteristic trait of the Néel spin-orbit torque switching in CuMnAs is its amplitude which was experimentally achieved in the order of $0,1\%$ of the sheet resistance. This is corresponding to the CuMnAs thin-film AMR coefficient, which is $0,2\%$ [11]. This is quite important for distinguishing this effect from the quench switching described in the next section.

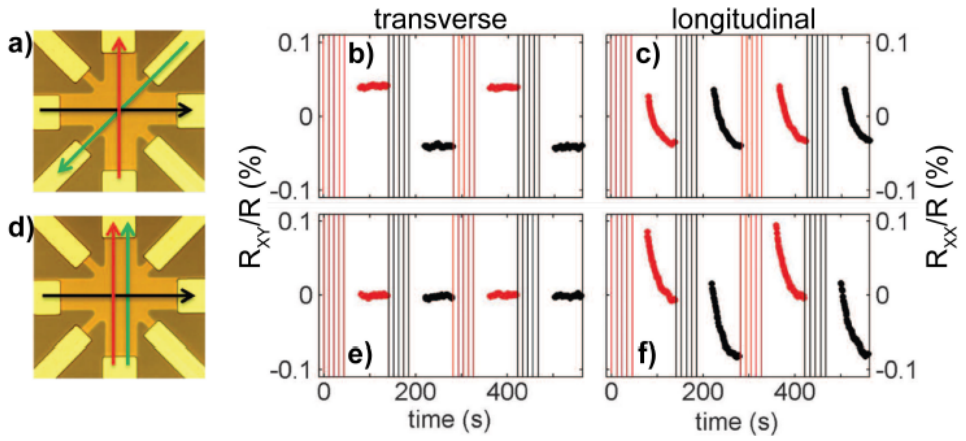

Figure 1.9: Reorientation switching in CuMnAs. a) Diagonal readout configuration. The probing current direction (green) is diagonal to the directions of writing pulses (red and black arrows). b), c) Corresponding transverse and longitudinal resistance measurements. d) Parallel readout configuration. Probing current is along one of the two writing pulses. e), f) Corresponding transverse and longitudinal resistance measurements. Adapted from [24]

1.5 Quench switching in CuMnAs

The effect of magnetic domain fragmentation occurring in CuMnAs films when using electrical pulses with high intensities or strong optical pulses was named quench switching [1]. With the application of these pulses with high enough energy densities, the antiferromagnet is brought near its magnetic transition point called the Néel temperature. Then is quickly quenched into a nano-fragmented domain state. Experiments in [1] show that the system retains its nano-fragmented state over much longer timescales (by multiple orders of magnitude) than the time for which the system is in the transient state connected with elevated temperature.

The change in resistivity of CuMnAs resulting from Quench switching can be as big as 100% at low temperatures and can reach tens of percent at room temperature.

This process is different from a traditional AMR switching due to the Néel vector reorientation. Recent measurements suggest the coexistence of both effects [26], but the quench switching mechanism does not exhibit changes in high magnetic fields. In the case of CuMnAs, Néel vector reorientation takes place in the magnetic field of 2 T [12] while measurements from XMLD-PEEM indicate that nano-fragmented state was retained even after application of 7 T magnetic field. Measurements published in [1] and [2] suggest that this behavior is highly reproducible and universal between all CuMnAs samples.

This quench switching was rigorously characterized using electrical pulses for excitation. It was demonstrated using optical excitation as well. These initial experiments were performed with a small laser spot. They used a train of femtosecond laser pulses in order to produce a sizable response.

The quench switching effect comprises multiple components characterized by their amplitudes and characteristic relaxation times. All components follow the

Kohlraush stretched exponential function 1.11 [27], which is used to describe the behavior of the complex systems.

$$\Delta R(t) = Aexp\left[-\left(\frac{t}{\tau}\right)^{\beta}\right] \tag{1.11}$$

Where ΔR represents the resistance change caused by its respective component, A represents the amplitude and τ relaxation time of the said component. The stretched exponent $\beta = d/(d+2) = 3/5$ is related to the 3 dimensional system. Components usually observed in quench switching are the normal component and the negative fast component. The negative fast component is characterized by its smaller amplitude with a negative sign, sooner onset, and faster relaxation time, which is in the range of tenths of a second. The normal component dominates the quench switching mechanism with its much higher amplitude. It can be distinguished from the negative component by its relaxation time of approximately 10 seconds at room temperature.

Microscopic origin of this new effect was recently debated [1] [26]. The experiments show that with the application of a high current electrical pulse or strong optical pulse, the system is heating up to the vicinity of the Néel temperature, which is 480±5K in case of the CuMnAs [28]. During the heat application (electrically or optically), no signs of electromigration or structural transition of the crystal were observed. This is supported by the fact that the range of optimal growth temperatures of CuMnAs (190-260 °C) well exceeds its Néel temperature. Even with this high temperature and much longer timescale (tens of minutes), the synthesized epilayer shows full crystal order[3].

1.5.1 Magnetic domain fragmentation

Nano-fragmented state in CuMnAs after application of strong electric pulses was observed using multiple magnetic microscopy techniques [1].

Figure 1.10 shows domain fragmentation observed by x-ray magnetic linear dichroism (XMLD) photoemission electron microscopy (PEEM). In figure 1.10a is shown the virgin domain configuration of CuMnAs. Micrometer large domains are clearly visible, and their perpendicular orientation indicates biaxial magnetic anisotropy in the material. After application of a strong electric writing pulse with a current density of $10^7 A.cm^{-2}$, the fragmentation occurs, and large domains are split into tiny new domains as shown in figure 1.10b. Results indicate that this fragmentation occurs only in the areas with high current density pulse present. More detailed images of the center part of a similar device are shown in figure 1.10c and d.

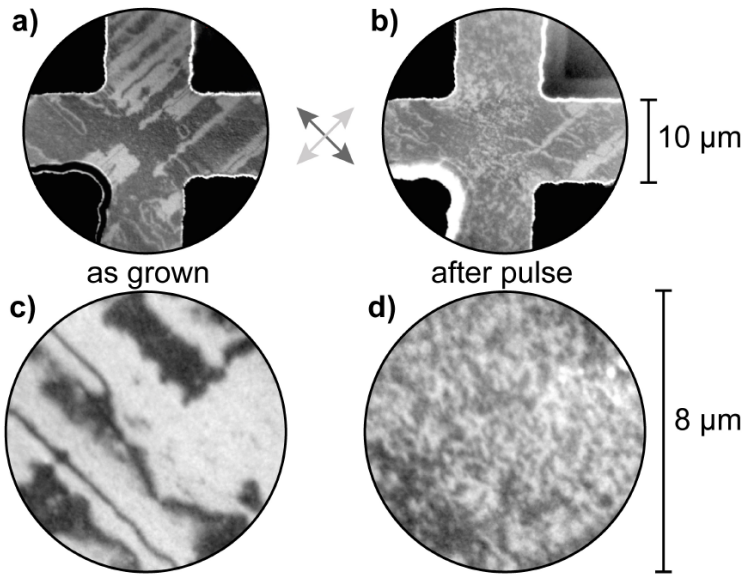

Figure 1.10: XMLD-PEEM observation of domain fragmentation. a) Virgin large magnetic domain state. b) Fragmented domain state after applying strong electrical current pulse between upper and lower arm of the device. c) and d) are analogous high resolution images of central part of the different device on a same material. Adapted from [1].

These images show how large the change in the domain size is. The typical size of the fragmented domains is well below the 100 nm resolution of XMLD-PEEM.

Theoretical calculations predict antiferromagnetic domain walls with widths around 100 nm depending on the strength of the magnetic anisotropy and exchange interaction. Domain walls of these widths are observed by the XMLD-PEEM [29], but only for virgin (relaxed) samples with large domains. Very recent measurements suggest a new type of atomically sharp domain walls, which was an unexpected result, whose theoretical description is not yet available [30].

1.5.2 Nanometer scale domains

The recent STEM DPC measurements (scanning transmission electron microscope with differential phase contrast) provided clues to understanding the nanometer-scale domains in the nano-fragmented state. STEM DPC is sensitive to the magnetization of single atoms. Magnetic domains in CuMnAs were measured and showed atomically sharp domain walls [30]. Images from this measurement can be found in figure 1.11. Image a) shows a signal from the HAADF detector, which is sensitive to atomic mass and shows a perfect crystalline structure. Image b) shows the DPC signal, which is sensitive to a beam deflection caused by interaction with the magnetic moment of each atom and captured by a four-quadrant detector. It shows an atomically sharp transition between two domains.

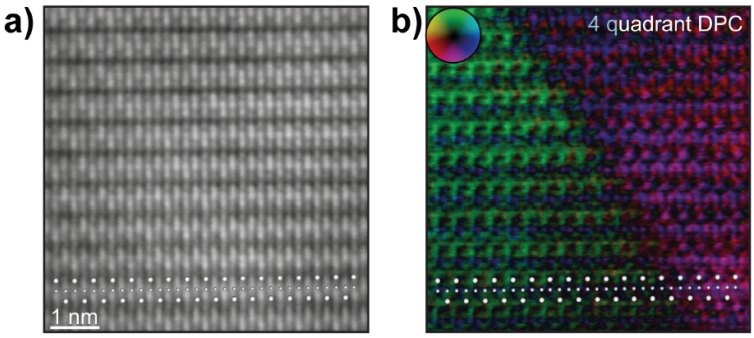

Figure 1.11: Image of thin domain wall measured by STEM. a) HAADF image, where contrast corresponds to atomic mass. b) DPC detector signal, where colors represent electron beam deflection. Adapted from [30].

1.6 Femtosecond laser pulse interaction with thin CuMnAs films

In this section interaction of laser pulses with thin CuMnAs films will be explored. With $\approx 150fs$ laser pulse directed at the air-CuMnAs boundary there are three major effects taking place [31] [32]. Firstly, the electrons in CuMnAs are heated up, and a new thermalized electron system is created. This hot-electron system can be characterized by a Fermi distribution with an electron temperature T_e, and it is formed within $\approx 100fs$ after the impact of the laser pulse. Secondly, the excess energy needs to be dissipated into the lattice from this electron system. This takes place on a picosecond time scale and is moderated by electron-phonon scattering. This scattering leads to an increase in temperature of the CuMnAs lattice T_{lat}. A side-effect of this energy transfer from electrons to phonons (magnons) is thermal stress that can create coherent acoustic wavepackets (strain waves) in the substrate of CuMnAs film. The third effect is classical heat diffusion which happens on a longer time scale and brings the whole system back to equilibrium.

All of these effects lead to change in optical properties and were measured recently on different CuMnAs films grown on GaP substrates [33]. Differential reflectivity and its dynamics were measured. It follows this phenomenological equation [32]

$$\Delta R/R(\Delta t, \lambda) = [\alpha(\lambda)(1 - e^{-\Delta t/\tau_{ee}})e^{-\Delta t/\tau_{ep}} + \beta(\lambda)(1 - e^{-\Delta t/\tau_{ep}})]e^{-\Delta t/\tau_{th}} \quad (1.12)$$

The first term of this equation represents the response of the electrons with a spectral weight α, rise time determined by electron-electron thermalization time τ_{ee} and decay by thermalization to the lattice with electron-phonon relaxation time τ_{ep}. The second term represents lattice heating. It has a spectral weight β, and it has the same rise time as decay time for electrons τ_{ep} because of the energy transfer between the electrons and the phonons in the lattice. Thermal relaxation time τ_{th} represents the heat diffusion into the surrounding area.

Measurements done in [33] have shown that the characteristic time scale needed to reach equilibrium for 10 nm film was $\approx 10ps$ with similar results for different thicknesses.

Electron-phonon relaxation time in CuMnAs was determined as $\tau_{ep} = 2,4 \pm 0,3ps$, which is comparable with characteristic times of Au ($\tau_{ep} = 1ps$ [31]). One of the most important results of that study was the determination of dissipation dynamics. It was shown that it follows monoexponential decay for long time scales.

For better understanding, additional computer simulations were performed in Comsol Multiphysics. Laser pulse was simulated as 150 fs square shape with constant power density in the CuMnAs layer. The ambient temperature was set to 15 K, and the average temperature inside the CuMnAs layer was simulated. A Debye model was used for specific heat capacity. Exact parameters can be found in [33]. Results in figure 1.12c are showing that the relaxation time describing the heat dissipation is growing with increasing thickness and reaching 2 ns for 60 nm thin CuMnAs film.

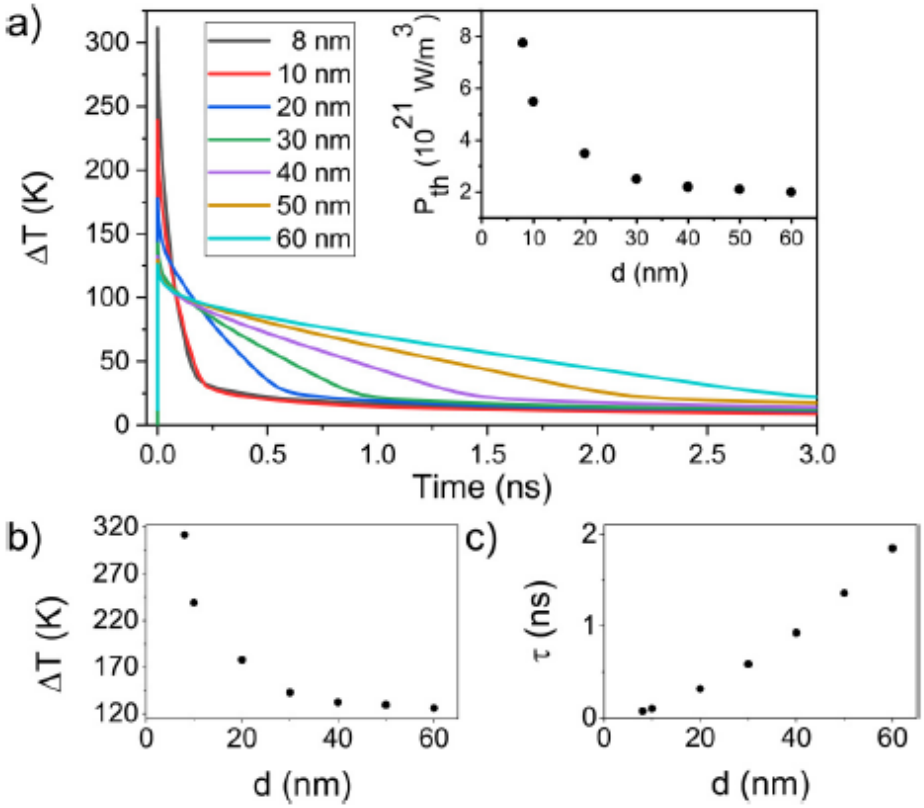

Figure 1.12: Heat transfer simulations in CuMnAs films of different thicknesses. (a) Transient change of CuMnAs temperature increase ΔT, relative to the sample base temperature of 15 K, computed for denoted film thicknesses. Inset: absorbed effective power density used in simulations for individual film thicknesses. (b) and (c) Dependence of the initial value of ΔT (b), and effective thermal relaxation time τ (c) on the film thickness. Note that at elevated sample base temperature, the values of ΔT would be smaller due to a strong temperature dependence of the heat capacity. Adapted from [33].

2. Sample preparation and experimental methods

This chapter will provide a technical description of the manufacturing process for CuMnAs devices. Its purpose is to give the reader insight into the techniques required for replication of this work.

In the first section, the growth of the CuMnAs film using the Molecular Beam Epitaxy (MBE) system will be explored.

The second section is dedicated to device fabrication using electron beam lithography. All steps, including used recipes, will be described to the reader.

In the third section, device geometries and their parameters will be discussed.

2.1 Growth of CuMnAs

Thin CuMnAs films are grown using Molecular Beam Epitaxy (MBE), one of the highest quality methods for thin film deposition with a low number of impurities. It uses ultra-clean materials and an ultra-high vacuum chamber (typically 10^{-12} Torr) which is pumped with multiple stages of vacuum pumps, including a helium cryogenic vacuum pump for the last stage. To keep the pressure low and stable during operation, the inner area of the growth chamber is equipped with nitrogen-cooled cryo-panels. Their freezing walls serve as natural sorption centers. Unwanted particles that would otherwise increase chamber pressure or serve as impurities in the grown material get caught on the cold walls of the cryo-panels.

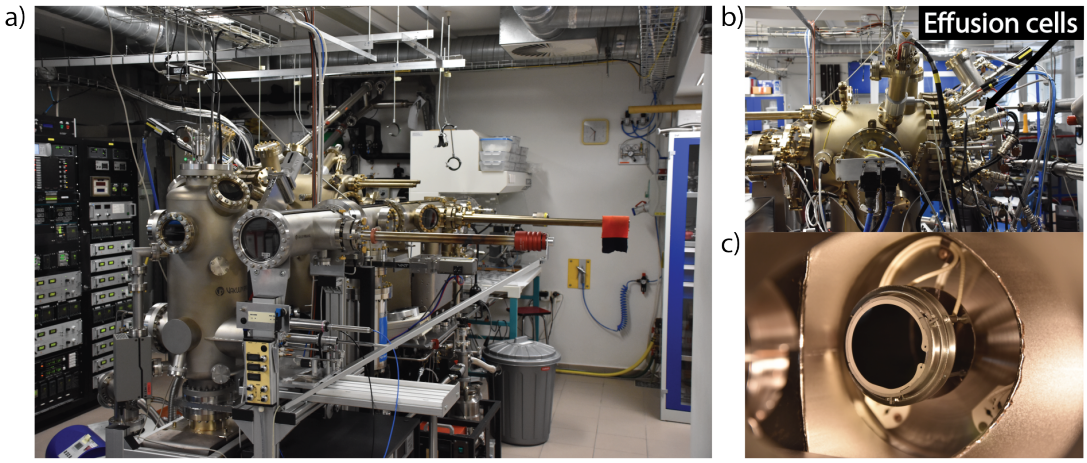

Figure 2.1: Veeco MBE system. a) Photo of the whole MBE system b) Growth chamber c) Substrate with its holder in the second bakeout chamber

In the case of this thesis, CuMnAs thin films were grown using the Veeco MBE system of the second generation shown in figure 2.1 a and b and in figure 2.2b.

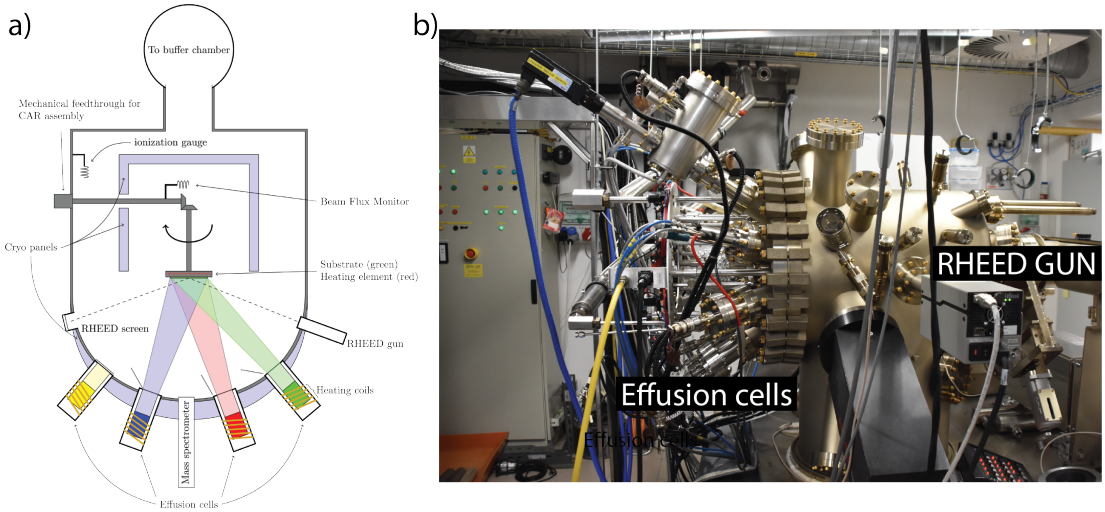

Figure 2.2: a) Schematic of typical MBE chamber b) Veeco MBE chamber used for growth in this thesis.

Every growth process in the MBE starts with a substrate preparation. The first appropriate substrate for MBE growth is loaded in a stainless steel wafer holder, placed on a transport trolley. In the case of the MBE used, all of this work is carried out in a flow box. The trolley can hold up to five two-inch wafers. The whole trolley is loaded in the load-lock, where it is baked out for the first time before it enters the transport tunnel. After entering the second bake-out station, individual substrates are picked with a transfer rod from the trolley and baked out in the separate chamber for 12 hours as shown in figure 2.1c. This process ensures that substrates are properly degassed and free from potential contaminants.

After this bake-out, substrates are ready to enter the growth chamber using transfer rods. Schematic of the growth chamber can be found in figure 2.2a, while a photo of the MBE chamber used can be found in figure 2.2b. The substrate in the wafer holder is attached to a rotating stage, which is orientated in a correct position to the effusion cells. Rotation of the wafer holder helps to compensate for a slight angle between the axis of the substrate and material flux coming from the effusion cells. The surface temperature of the substrate is then monitored by optical band gap spectrometry.

When the growth process is started, individual effusion cells are heated up to their working temperatures. This causes an emission of an atomic flux of one pure material. By varying the temperature, the atomic flux can be regulated to obtain the optimal growth rate. The whole effusion cell is capped with a shutter which is open only during deposition.

The growth rate is monitored by the reflection of high-energy electron diffraction (RHEED). This method uses an electron gun pointed at a shallow angle on the substrate, and a fluorescent screen with a camera is used to visualize a diffraction pattern. Electrons diffract at the surface of the substrate (or growing atomic layers), and the diffraction pattern oscillates depending on the atomic structure and its coverage of the surface. One period of the oscillation corresponds to one monolayer grown. In order to identify possible contaminants and leaks during growth, the growth chamber is equipped with a mass spectrometer.

At the start of the growth process, the native oxide has to be removed from the substrate. In order to remove it, the substrate is heated up to 650°C for GaAs and GaP, and over-pressure of As od P respectively is created. This over-pressure prevents evaporation of As or P from the surface. Then the growth process can start with the calibration of cell temperatures. This calibration is done by measuring the beam flux directly by inserting a special tool in front of the substrate or by monitoring the growth rate on the substrate using RHEED. This calibration is very specific to each MBE system. It is not very precise but is mandatory to achieve for materials where layer by layer growth is hardly achievable (Cu in case of the CuMnAs).

In order to improve the first layers of CuMnAs, the surface of the substrate is smoothed out by growing a 50 nm thick buffer layer of GaAs od GaP depending on the substrate used.

The CuMnAs films studied in this thesis are well optimized and grown at temperatures between 210 and 220°C. Slight temperature overshoot of 10°C at the beginning of the growth process is due to increased heat absorption in the CuMnAs compared to the substrate [34] and by heat generated when opening

the shutters of the heated effusion cells. The usual growth rate is 1.2 unit cells per minute, and it is controlled by regulating the Mn and Cu beam fluxes. Beam flux of As is self-regulated.

After deposition of the desired thickness of CuMnAs film (20 or 50 nm in case of samples in this thesis) sample is passively cooled by surrounding cryo-panels below 0°C. At this point, an aluminum capping layer with a thickness of 3 nm is deposited. This thickness is optimized to oxidize in the ambient environment fully while preventing CuMnAs oxidation. Thanks to this optimization capping layer has only a negligible impact on overall conductivity.

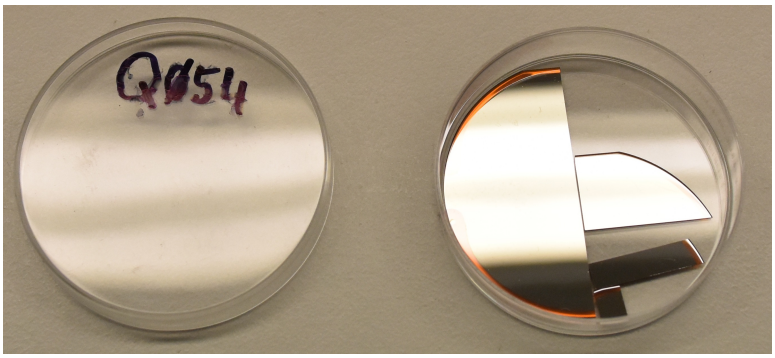

Figure 2.3: Example of CuMnAs thin film grown on GaP substrate wafer. This wafer is then cut into individual samples.

More detailed information regarding CuMnAs growth can be found in this recent paper from our group [3].

2.2 Lithographic device fabrication

All devices used in this thesis were prepared using electron beam lithography (EBL). Typically characterization devices are also prepared using masked optical lithography, but because of specialty designs and higher requirements on precise alignment, EBL was chosen for all devices.

All fabrication was performed in the cleanroom, where all air is highly filtrated and purified, decreasing the floating particle count significantly. This air filtration is necessary to ensure successful lithographic processes where individual exposed features are comparable in size with floating particles in the air. Cleanrooms can be classified by a numerical value, which usually refers to a number of particles larger than 0.5 μm in one cubic meter. Our cleanroom is classified as a 100 in the area next to the electron lithograph. The surrounding areas where resist films are prepared are classified as a 1000 and the separate room with plasma etching and vapor deposition machines as a 10 000.

In the cleanroom, yellow light is used in order to prevent premature exposition of UV-sensitive resists while handling the samples. Therefore, all lights are equipped with filters that block the high-energy part of the spectra and turn all lights to yellowish color.

The lithographic process is shown schematically in figure 2.4. The process starts with cleaning of the sample either in an acetone bath followed by an isopropyl alcohol (IPA) bath or oxygen plasma followed by the acetone and IPA,

in case more thorough cleaning is required. The recently grown samples have a spotless surface, and even unnecessary standard cleaning processes may lead to their contamination.

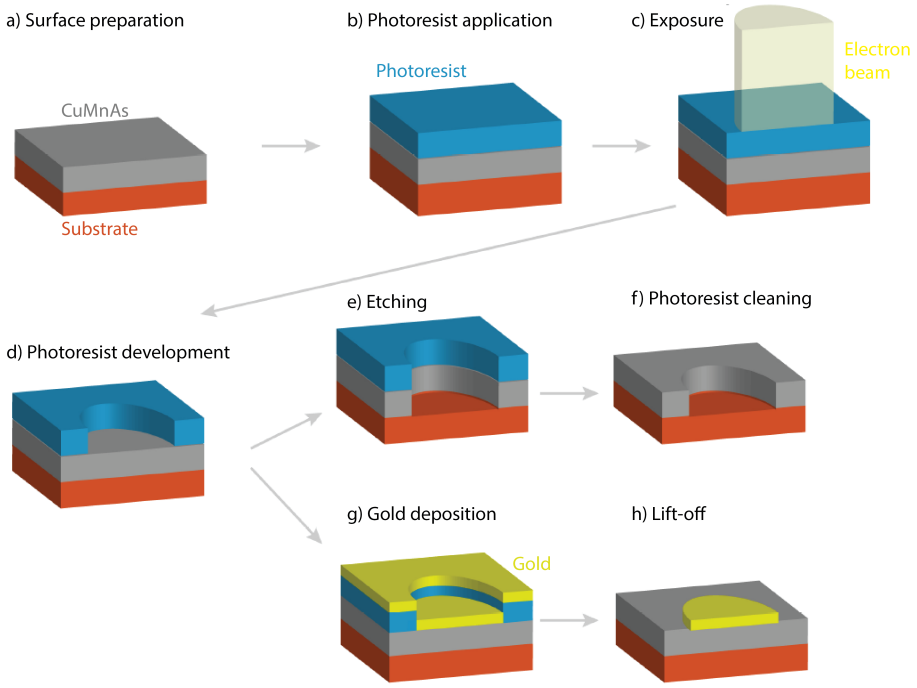

Figure 2.4: Schematical representation of lithography. a) Sample is cleaned using acetone and IPA. b) Photoresist is applied using the spin-coating technique. c) An electron beam exposes the features. d) Photoresist development. In the case of a positive photoresist, the exposed area is removed. e) CuMnAs is etched away in the exposed areas. f) Photoresist is cleaned using an acetone bath. g) Gold is vapor-deposited on top of the photoresist. h) Photoresist is washed away during lift-off along with excess gold. Adapted from [2].

After cleaning, an electron beam-sensitive resist is deposited on the surface of the sample. Before each use, resists have to be filtered using a centrifuge to get rid of hardened particles in the resist. Afterward, the resist can be applied to the surface of the sample and spun with a spin-coating machine (shown in figure 2.5 a). This high RPM spinning cycle (usually 5000 RPM for 45s) ensures the homogeneity of the resist film. It is good to note that this applies only to a center part of the sample since edges are a natural barrier for the resist, and therefore the film is thicker in the region 0.5 mm from the edges. After the spin-coating process, the resin needs to be dried out using a hot plate.

When the resist application is finished, electron beam lithography (EBL) can be performed. The EBL machine used for the sample exposure in this thesis was a modified RAITH E-Line Scanning Electron Microscope (SEM) machine (shown in figure 2.5 b). This method allows the preparation of unique designs, and it is suitable for the iterative process of improving the devices. The resolution is given by a combination of electron beam properties (extraction voltage, aperture size, etc.) and selection of resist (thickness, exposure rate, etc.). In the setup used for

this thesis minimum feature size is about 100 nm.

Samples are held on the special holder, which is then loaded into the EBL machine using a load lock to prevent loss of the vacuum. After the loading process, several tasks have to be performed to start the exposure. In the first task, beam current has to be measured using a Faraday cup on the holder. Then sample has to be located, and its angle has to be recorded to be compensated afterward. Next, the beam has to be focused using some specs of dust on the sample's surface. During the focusing routine, the writing fields are also aligned in multiple steps, increasing the precision of the alignment. Lastly, the exposure parameters can be calculated, and the exposure process can be started. During the exposure process, the area of the sample is divided into writing fields. In each writing field, a pattern is exposed by tilting the electron beam and shuttering it in the places where the exposure is not desired. After the exposition of one writing field sample holder moves into the next location of the following writing field.

Exposition changes the properties of resists. Polymeric chains are broken up by the energy delivered by an electron beam. That also changes the chemical reactivity of the resist, and therefore exposed parts can be washed out in a proper development solution. There are two types of resists classified according to their behavior after exposition - positive and negative resists. Positive resists open up in the directly exposed places, and negative resists open up everywhere else.

For device fabrication in this thesis, two types of electron-sensitive resist were used - PMMA A4 and A6. Both of them are positive electron-sensitive resists, but they differ in their viscosity and, in turn, in their final thickness. The A4 photoresist is spun to a thickness of 200 nm, while the thickness of the A6 is typically 300 nm. Both resists are then dried using a hot plate set to 130°C for 2 minutes. The exposure dose for both resists is the same 120 $\mu C/cm^2$ with 10 keV accelerating voltage. The usual writing field is 100 μm square, and beam aperture is set to 30 μm, which represents a beam current of 210 pA. In case of exposing large areas with lower precision writing field of 200 μm and beam aperture of 60 μm, corresponding to 900 pA is used.

Development of both resists is done in a solution of MIBK:IPA 1:3 for 35 seconds. Etching of CuMnAs is then performed either with acid solvents (wet etching) or by reactive ions (dry etching). Before the etching process, the aluminum cap has to be removed by dipping samples in a solution of 2.7 % TMAH (Tetramethylammonium hydroxide $C_4H_{13}NO$) for 10 s. Usually, wet etching of CuMnAs is used in this thesis. This process is done either in solution of $H_3PO_4 : H_2O_2 : H_2O$ in ratio 1 : 10 : 400 or in solution of $C_4H_6O_6(5\%) : H_2O_2(5\%) : H_2SO_4(10\%)$ in ratio 4 : 1 : 2. For both solutions etching speed is roughly 60 nm per minute. A good indication of successful etching on GaP substrate is its transparency. When CuMnAs film is removed completely sample one can see through the GaP substrate. On other substrates, etching has to be verified by using a surface profiler, e.g., Dektak by Veeco (shown in figure 2.5 d).

After successful etching, the next step is to create contact pads. That involves the second layer of lithography with all the steps mentioned above. One crucial thing is the alignment of contact pads onto an existing device. That is why all designs incorporate alignment crosses in multiple places in order to provide a choice of alignment for second or third lithography. After developing the resist,

Figure 2.5: Different machines used in lithographic process. a) Spin-coating machine with hotplates behind it. b) Raith E-line electron beam lithography machine. c) Vapour deposition machine. d) Dektack surface profiler.

samples are dipped into TMAH for 10 s in order to remove Al capping layer and then quickly transferred onto the holder for the vapor deposition machine (shown in figure 2.5 c). Standard contact pads use gold, thanks to the gold's high conductivity and non-oxidizing properties. However, there is a problem with placing Au on CuMnAs, so more reactive metal has to be used as a thin spacer layer. Here we are depositing 5 nm thick film of Cr, and then we deposit another 75 nm of Au. In order to have successful lift-off, deposited material cannot be thicker than the resist layer. That is the reason why thicker A6 resist is used for metal deposition.

The last step for standard devices is the removal of the resist. This is usually done in an acetone bath, but some special cases require unique solutions like Xylene (dimethyl benzene $(CH_3)_2C_6H_4$). This process also washes away the excess gold from the resist-covered areas.

2.2.1 Device contacting

Finished devices on the sample need to be contacted to the holder PCB (printed circuit board). First of all, samples are glued to the PCB using thicker A8 resist, which is then dried using the hotplate at 110°C for 2 minutes. When the sample is fixed in place, it can be contacted using the bonding machine. It uses 30 μm thick Al wire to connect the contact pads of the devices to the contact pads on the PCB. This contacting is done by squishing the Al wire with set force and ultrasonic vibrations. Bonder used for contacting devices used in this thesis was Kullicke & Soffa (K&S) 4123 ultrasonic wedge-bonding station and is shown in figure 2.6.

After contacting, all connections are checked with a multimeter to verify the connection and prevent possible shorts. Connections have to be also checked before measurement because the bonding wire can come loose during transport.

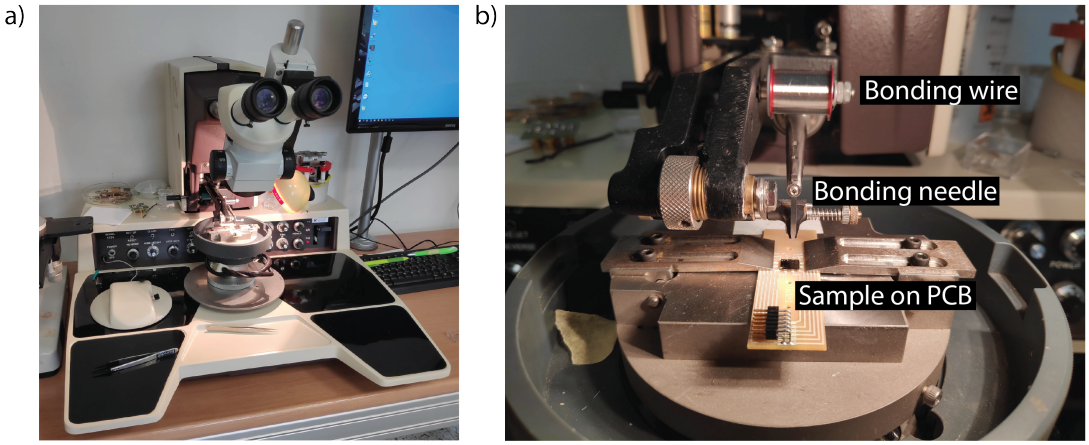

Figure 2.6: Photos of ultrasonic wedge-bonding station. a) Photo of a whole station. b) Detail of an inserted sample.

2.3 Device types

During preparation for the measurements of this thesis, a few different device designs were explored. In the end, as the best choice was determined, a hall bar design comprising of just one square, which was either 20 or 10 μm wide. This design was chosen with regard to the used laser spot, which could be set to 20 μm or more. Devices with the larger active area were not used for two reasons. The first reason was to ensure the possibility of using a bigger laser spot, thus ensuring more homogeneous illumination. The second reason was to maximize the ratio between the quench switched region and the whole bar. The dependency of the quench switched region will be explored in section 4.2.4.

As mentioned above, for the standard measurements, the square hall bar was used. It was comprised of a 10 or 20 μm square with 3 μm wide hall probes. These were symmetric on both sides in order to make bonding easier. A 3D model of such device with comparison to the actual device image from the optical microscope is shown in figure 2.7. Reading current flows along the red arrow, and resistance of the square is read with the hall probes labeled V+ and V-. These one square hall bars are distributed on the whole sample with variations. This is done to ensure the possibility of measuring different crystallographic directions.

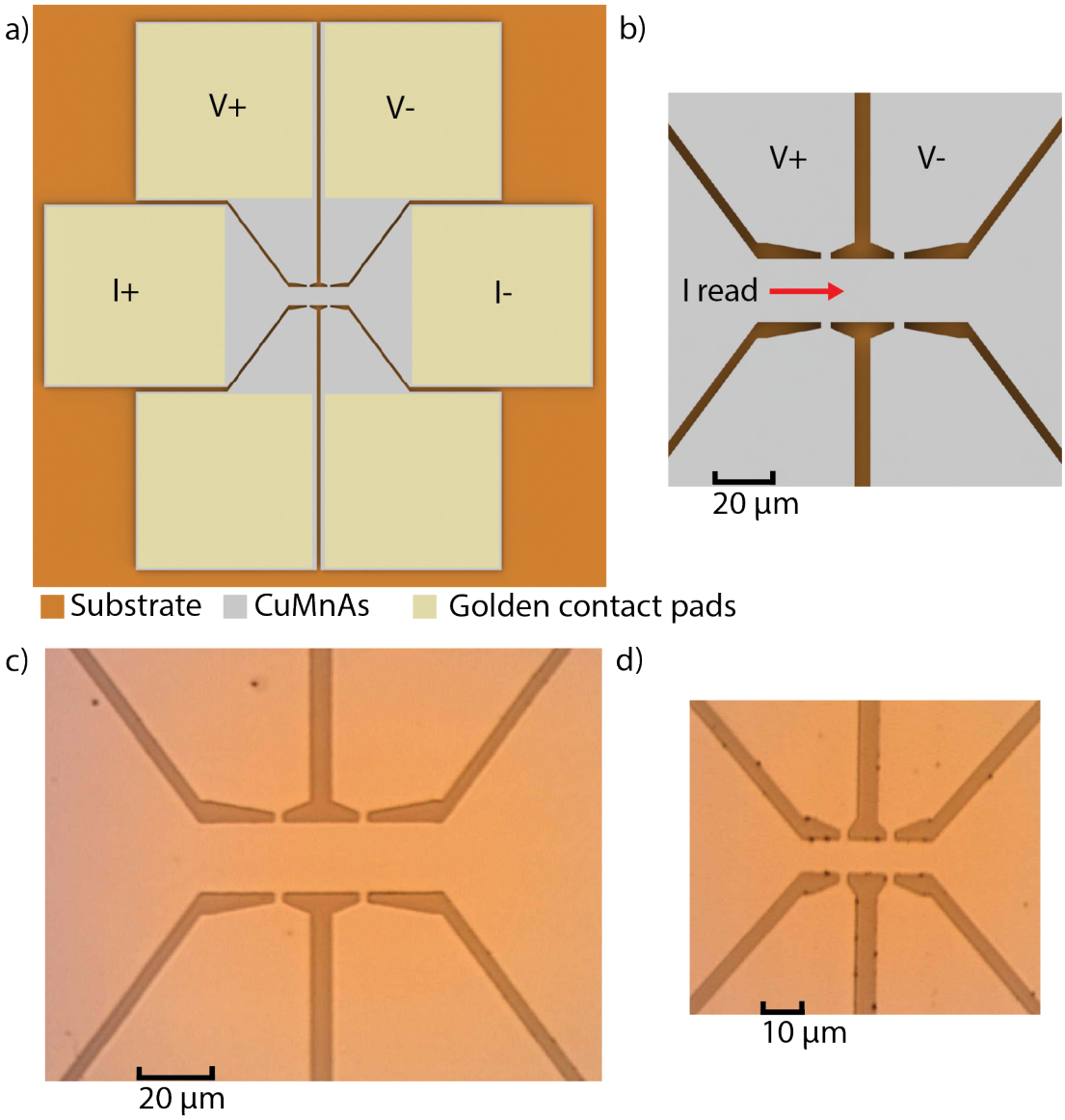

Figure 2.7: 3D renders and microscopic images of standard devices. a) 3D render of 20 μm single square hall bar. b) Detailed render of the device center. c) Microscopic image of 20 μm single square hall bar. d) Microscopic image of 10 μm single square hall bar.

During this thesis, more intricate measurements were also performed. These aimed to quantify the quenched area switched with given laser intensity and gauging the positional dependency of switching. In order to measure it on a distinct border special design of a double square hall bar was used. This design consists of two squares in series with the capability of independent measurement for both squares. The width of the conductive channel is 20 μm, and the whole device with its model and actual image from the microscope can be found in figure 2.8. Reading current flows along the red arrow and the hall probes are now distinguished as V_1+,V_1-,V_2+ and V_2-.

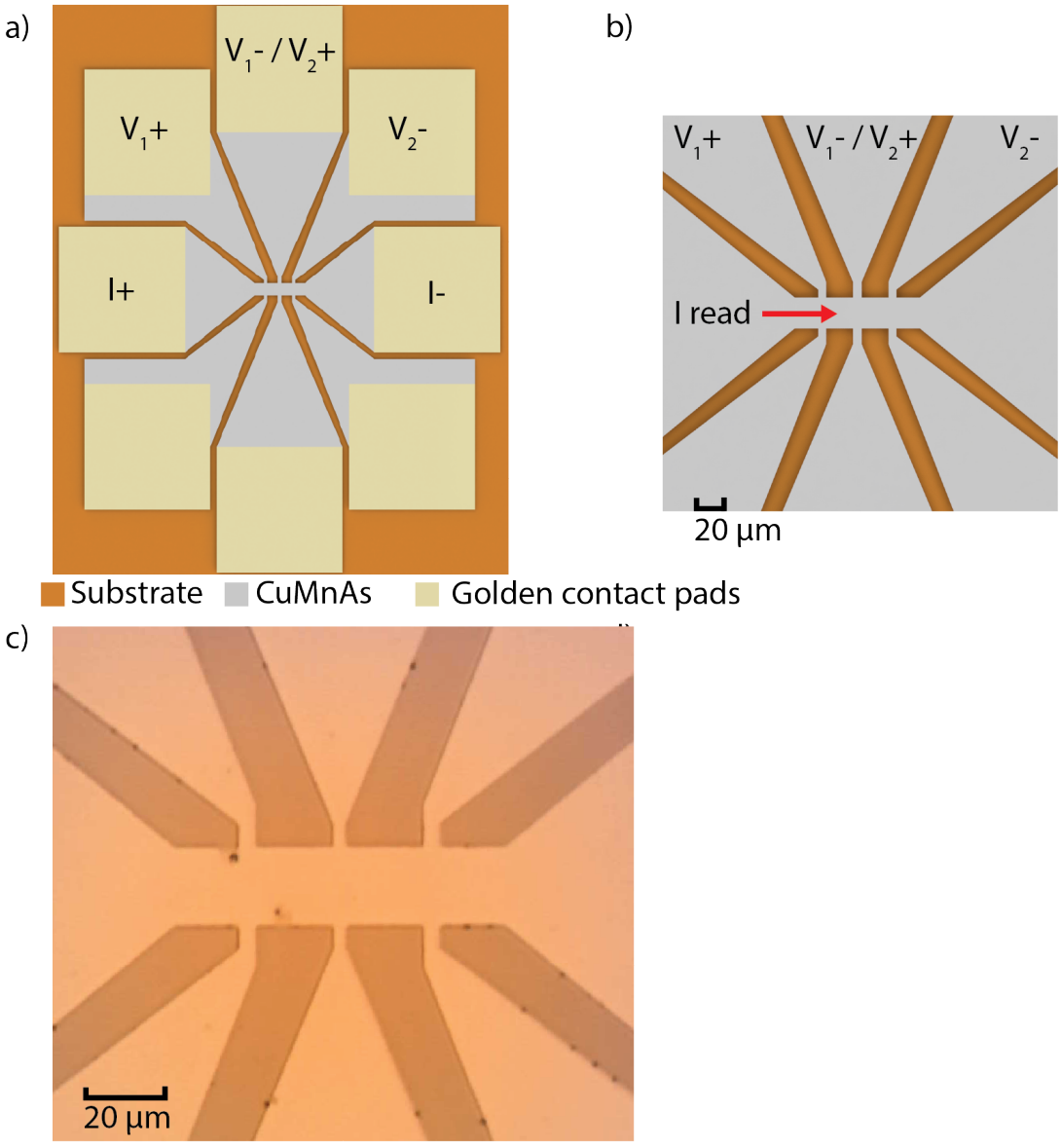

Figure 2.8: 3D renders and microscopic images of double square hall bar device. a) 3D render of the whole device. b) Detailed render of the device center. c) Microscopic image of the center part of the device.

3. Measurement setup

This chapter will present the important attributes of the used measurement setup.

The first section is dedicated to the detailed explanation of the used components and the reasoning behind their choice. It will also provide a detailed explanation of the calibration techniques used to prepare the experimental setup. Schemes and photos will give an overview of the actual arrangement of used components.

The second section will show the steps taken before the measurement. It details the procedure that needs to be taken after changing the measured device or the whole sample.

3.1 Electro-optical setup overview

In order to properly measure data for this thesis, an electro-optical measurement setup was constructed. This was done in order to allow the optical excitation with an electrical readout of the devices. This is the most favorable configuration, thanks to significant changes in electrical resistivity of CuMnAs as a result of the optical excitation. Optical responses, such as changes in reflectivity, are smaller and require a more complicated optical configuration to detect. Therefore this combined electro-optical measurement is the most straightforward configuration with the ability to detect changes caused by optical excitation while having a reasonable signal-to-noise ratio.

3.1.1 Optical excitation

The cornerstone of the optical part of the used setup is the femtosecond laser system Pharos manufactured by Light Conversion, which is shown in figure 3.2a. This laser system works at the wavelength $\lambda = 1030$ nm with variable resonator frequency. For the measurements done in this thesis, the laser system was set to the resonator frequency of 190.2 kHz. This corresponds to the 10 W of the continuous laser power of the resonator and single pulse energy of 53 μJ. The output of the resonator then passes through a pulse picker, which is an electro-optical modulator, which can discard unwanted pulses. The last stage of the laser system is the beam splitter, which splits the output between the optical parametric amplifier and the free space output in the ratio of 8:2 in favor of the OPA. So in the case of the pulse picker in the open setting, usable continuous power on the free space output is 2 W, which corresponds to the laser pulse energy of 10.5 μJ.

A simplified schematic of the optical arrangement is shown in figure 3.1. The output from the laser system is directed through a mechanical shutter. This, combined with the pulse picker on a set division rate, allows to do single pulse experiments or use a well-defined train of pulses. A combination of both is easier to control and synchronize via the computer because using just the laser system with its pulse picker is difficult to interface and synchronize with the rest of the experiment. For the single pulse experiments, the pulse picker is set to a division of 1902, which corresponds to a 100 Hz frequency of the laser pulses coming from the laser system, and the mechanical shutter is set to an open time of 15 ms. This window ensures that just one pulse will pass through, which was rigorously tested.

From the shutter's output, the laser beam is then divided using a beamsplitter (BS 1) into a pump and a probe beam. For purposes of this thesis, only the probe beam is used, and therefore the pump beam will not be discussed in detail. The power of the probe beam is regulated using a rotating half-waveplate and a polarizing beamsplitter (PBS 1) at a point of the combination of the pump and the probe beams. The half-waveplate is rotated using piezoelectric rotator ELL14 from ThorLabs controlled via the computer. For purposes of this thesis, a special mount was designed and 3D printed, which allowed mounting the rotator. This mount is shown in figure 3.2b.

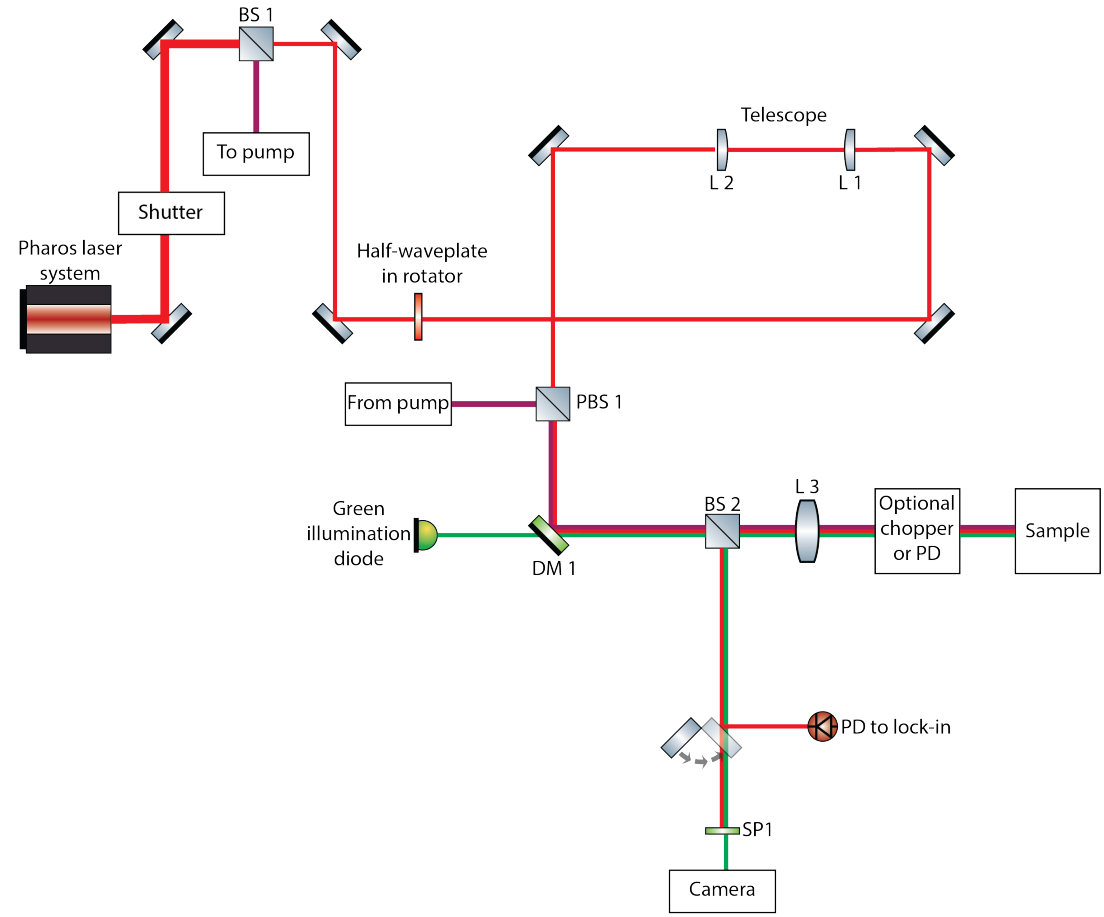

Figure 3.1: Simplified schematic of the optical setup used in this thesis. Optical chopper or a PD in front of the sample are present only during the beam characterization.

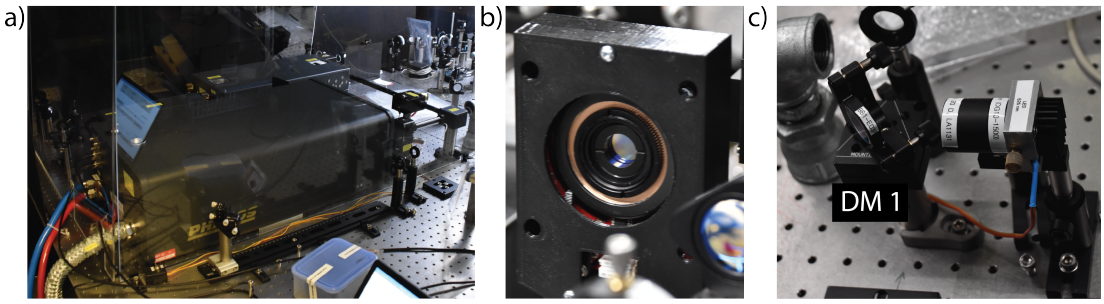

Figure 3.2: a) Pharos laser system b) ELL14 rotator with half-waveplate c) Collimated illumination LED with dichroic mirror DM 1

In between the rotator with the half-waveplate and the polarizing beamsplitter is a telescope comprised of two identical aspheric AR coated lenses (L1 and L2). This allows a beam divergence to be manipulated, which changes the point of focus on the sample. The second lens (L2) of the telescope is mounted on a mechanical stage with a micrometric screw for positioning. Then the probe beam is recombined with the pump beam, which was blocked during our experiments, in the polarizing beamsplitter (PBS 1) mentioned above. Before it is focused on the sample, the beam hits dichroic mirror (DM 1), which allows the addition of

the sample illumination using collimated LED light source with wavelength λ= 525 nm shown in figure 3.2c. Afterward, it passes through a beamsplitter (BS 2), which redirects the light reflected from the sample into the camera, shown in figure 3.3b.

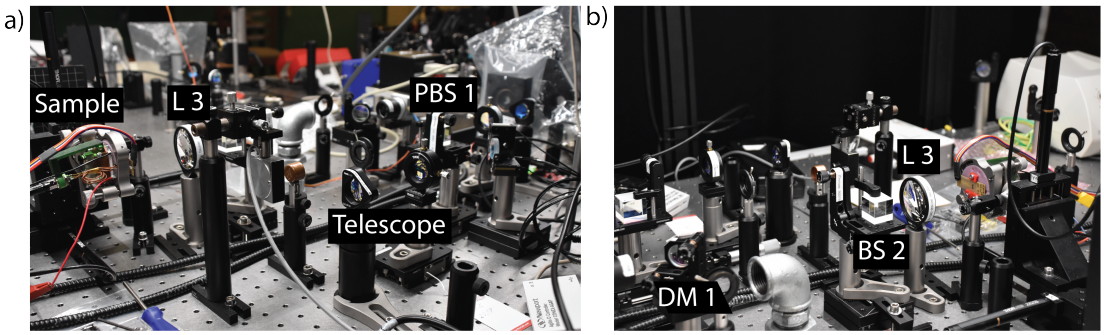

Figure 3.3: Photos of the sample space. a) Telescope and sample holder b) Beamsplitter BS 2 and focusing lens L 3

Lastly, the laser beam is focused onto the sample using an achromatic doublet lens with AR coating (L3) as shown in figure 3.3. This choice was taken over an objective lens because it allows a wider range of laser spot sizes on the sample (10-100 μm). It does, however, possess one significant drawback, which is its inability to compensate for astigmatism. This was apparent in our beam diameter measurements using the knife-edge technique, which will be discussed later.

3.1.2 Pulse energy measurement

In order to properly determine the laser fluence on the sample, two measurements have to be done. Firstly the power of the individual pulses has to be determined, and secondly, beam size has to be measured on the sample. In this section, the power measurement will be discussed.

The first step towards determining the pulse energy is to measure the average optical power at the sample. This was done by placing a photodiode power sensor in front of the sample and then running a power calibration as shown in fig 3.1. This consists of slowly rotating the half-waveplate and recording the average laser power on the photodiode power sensor. During measurements of this thesis as a power, the sensor was used Ge photodiode from TholLabs model S122C with a resolution of 2 nW and spectral range of λ = 700 - 1800 nm, which is well suited to the used laser light with λ = 1030 nm. Digital optical power meter model PM100D from Thorlabs was used as a readout for the photodiode. The output of this calibration is a calibration file linking the position of the rotator to the measured average optical power on the sample.

The second step is to calculate energy of a single pulse. Equation linking the average optical power P_{Avg}, repetition rate R_{rate} and energy of the single pulse E_{pulse} is this

$$E_{pulse} = \frac{P_{Avg}}{R_{rate}} \tag{3.1}$$

The usable range of optical power in the optical setup used for the measurements done in this thesis was P_{Avg} = 1 - 100 mW, which corresponds to a pulse energy of E_{pulse}= 5 - 525 nJ.

3.1.3 Spot size measurement

The laser spot size was measured using the knife-edge method, which required certain changes in the optical setup. In order to improve the signal-to-noise ratio, an optical chopper with lock-in measurement was used. Chopper was placed right in front of the sample, and its output was fed into the Stanford research system model 830D lock-in amplifier. Other change was redirecting the light from the camera using a mirror in the magnetic mount into the photodiode detector, which was also connected to the lock-in amplifier. Both changes to the setup are shown in figure 3.1. Since this measurement was done in the reflection geometry sharp transition edge between areas with different reflectivity had to be present on the sample's surface. This was accomplished by depositing a gold square with dimensions of 200 by 200 μm in the center of the sample. Different edges of the square can be used to check spot size in different directions.

Knife-edge method

Parameters of a Gaussian laser beam can be measured using the knife-edge method. In this method intensity of light on the detector is proportional to the position of the knife edge. If the edge is moving in the x-direction as shown in figure 3.5, intensity on the detector follows the equation 3.2 [35]

$$\begin{aligned} I(x) \approx \int_{-\infty}^{\infty}\int_{-\infty}^{x} e^{-2\frac{x'^2+y'^2}{w^2}}dx'dy' &= \int_{-\infty}^{\infty} e^{-2\frac{y'^2}{w^2}}dy' \int_{-\infty}^{x} e^{-2\frac{x'^2}{w^2}}dx' \\ &= \frac{\pi w^2}{4}\left(1+erf\left(\frac{\sqrt{2}x}{w}\right)\right) = \frac{\pi w^2}{2}\left(1-\frac{1}{2}erfc\left(\frac{\sqrt{2}x}{w}\right)\right) \end{aligned} \quad (3.2)$$

where erf and erfc are tabled functions, and w is the beam diameter.

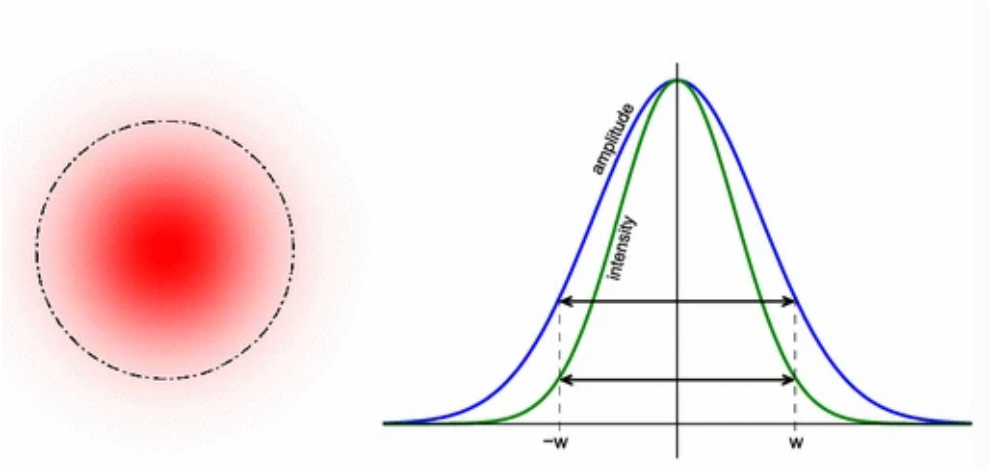

Figure 3.4: Example of Gaussian laser beam with its amplitude and intensity profile. Adapted from [36]

Positional dependence of intensity is acquired by a computer and then fitted with 3.2. Parameter w is the output of the fit. Example of the fitted data is shown in figure 3.6.

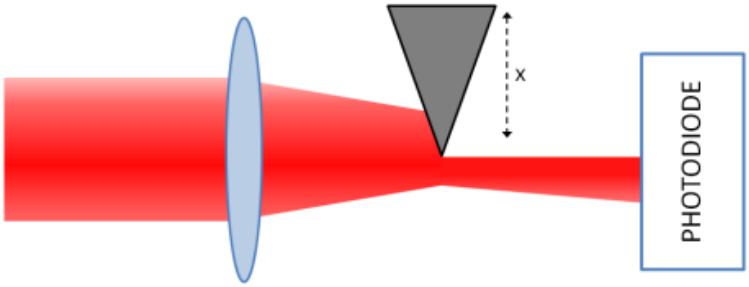

Figure 3.5: Schematic of the knife-edge method for measuring the beam diameter. Adapted from [37]

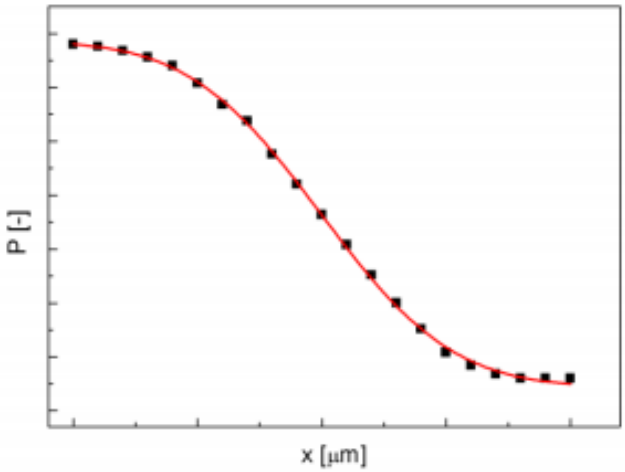

Figure 3.6: Example of the measured and fitted data using the knife-edge method. Adapted from [37]

Parameters of the laser spot were not optimal because the spot is not completely Gaussian. The knife-edge measurements have proven that the laser spot is astigmatic with a ratio of 2:3, with the exact size being 20 μm in the x-direction and 30 μm in the y-direction. This astigmatism was caused mainly by the final focusing lens. In the end, the decision was taken to match the laser spot as close as possible to the mentioned values on each measured sample as the spot will cover both 10 and 20 μm sized hall bars.

3.1.4 Electrical readout

The electrical readout was chosen because of its simplicity and high signal-to-noise ratio compared with the reflectivity measurements [2]. This influenced the design of the devices, as mentioned in the previous chapter.

The measured device was constantly supplied by a readout current from a Keithley Standard Series 2400 Source Measure Unit. Sourced current was set to 100 μA which is quite conservative and safe for devices with sub 50 Ω resistance. The readout of the voltage on the single square hallbar was accomplished by a Keithley 2000 Series: 6½-Digit Multimeter and Keithley DMM6500 6½-Digit

Graphical Touchscreen Digital Multimeter connected in parallel. This configuration is shown in figure 3.7. For a double square hall bar, each of the multimeters was measuring the voltage on one square.

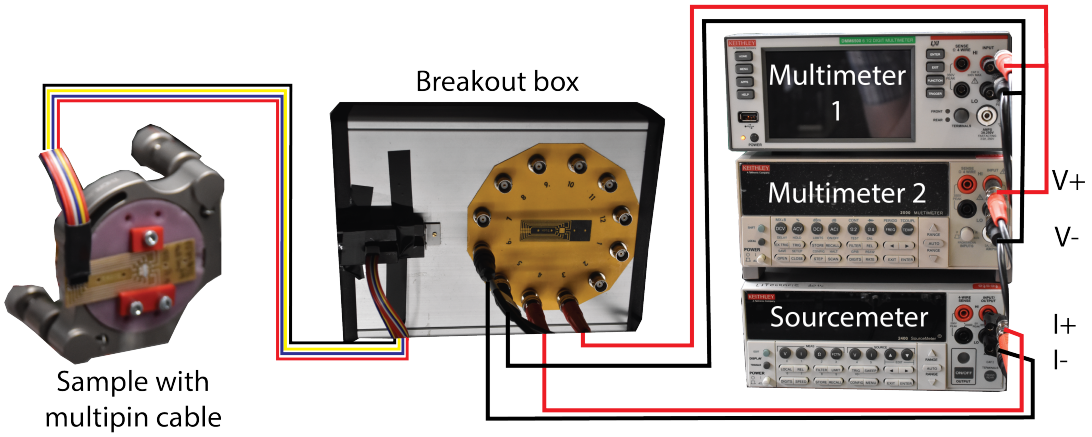

Figure 3.7: Sample electrical connection scheme used for measurements on single sqaure hallbar.

Parallel configuration was chosen for two reasons. The first reason was the possibility of measuring data with and without integrated filtering on the multimeters themselves and the second reason was consistency in formatting the measured data. One drawback of the parallel configuration is the halved internal resistance of the readout apparatus, which was still in the $G\Omega$ range. When considering devices with sub 50 Ω, the current flow through the multimeters was negligible.

Datapoint acquisition time was set to 20 ms on both multimeters, corresponding to one sine wave of the grid. This helps to mitigate the noise of the current source and the induction from the grid in nearby wires. Datapoints themselves were then pulled by the connected computer approximately every 250 ms.

Only 4 data points per second were enough to measure desired relaxation component. This work is focused on the normal relaxation component in CuMnAs, which has relaxation time around 7.5 s, and fitting this behavior is possible with this measurement setup. For measurements of the fast component, usage of the oscilloscope is planned.

3.1.5 Sample holder

For this thesis, a new type of sample holder was designed and manufactured. Final result is shown in figure 3.7. This specialty holder allows temperature stabilization of the samples using a Peltier module and a resistive heater wire. Sensing is done via the PT1000 temperature sensor. 3D model of this new holder with its section view are shown in figure 3.8.

As a basis of this sample holder was chosen Polaris side optic retention mount from ThorLabs in a 2-inch size. This stainless steel optic holder has increased temperature stability compared to standard optic mounts from the same brand.

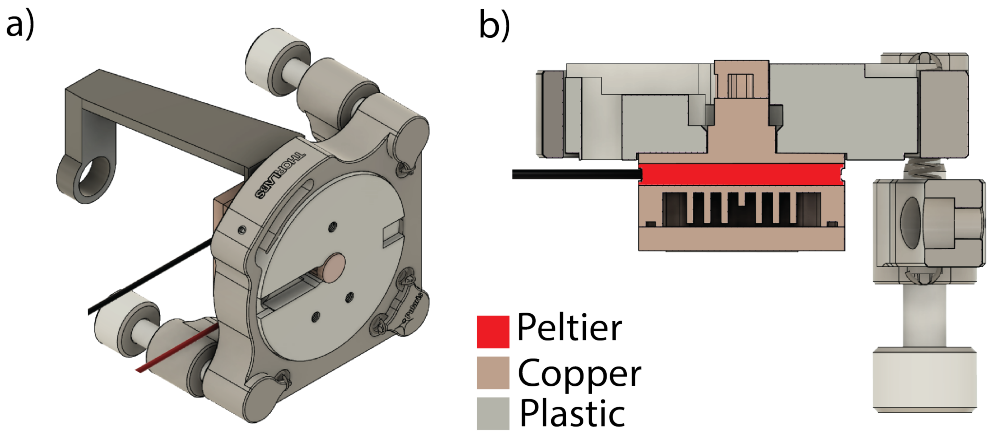

Figure 3.8: a) 3D model of the sample holder. b) cross-sectional view of the sample holder.

Special plastic housing for the cooling/heating components was designed. This housing was then 3D printed using Anycubic Photon S UV SLA resin printer with specialty high-temperature resin. DRUCKWEGE type D High Temp resin was chosen, thanks to its high-temperature stability and low expansion coefficient. The process of printing with this resin was difficult and had to be optimized before producing the final part. The main problems were with the adhesion to the printing platform and warping during printing.

Plastic insert houses special copper parts, which were designed to transfer heat to or from the sample. A two-part design was chosen to incorporate the possibility of a sensor swap and to allow the sensor to be mounted as close to the sample as possible. The internal copper part is also used as a base for the heater element, which constitutes three turns of resistive Manganin wire. This heater loop close to the sample allows finer temperature control. On the bottom of the larger copper piece is the Peltier element with dimensions of 30 by 30 mm. This is then cooled with a copper water block, which was also designed from scratch. All copper pieces were manufactured on a CNC router using a 1.5 mm endmill.

The water-cooling loop is created from readily available PC water-cooling parts. It uses pump and reservoir model Alphacool Eisstation VPP connected to a 120 mm radiator, which is more than capable of cooling down the Peltier module. Watercooling does not impose any negative vibrational forces on the holder, as was tested by a student working on a student project under the supervision of RNDr. Eva Schmoranzerová, Ph.D.. Holder was tested with the precision accelerometer and using interferometry.

All aspects of the temperature control are handled by a control box created for this thesis. It is based on the Arduino platform and uses precision AD modules for temperature readout. The control box is connected to the PC via the USB serial port. All other devices, including the holder, lab bench power supply for the Peltier module, and pump with a cooling fan on the radiator, are controlled by the control box itself. The heater element is controlled in a fast PID loop, while the Peltier module uses only proportional control due to the slow change speed of the lab bench power supply.

As a result, this holder can reach and hold temperatures from -30°C up to 60°C. Condensation and later ice formation is a significant problem for the tem-

peratures under 14°C; therefore dry-air enclosure was ordered. Although it was available during the measurements of this thesis due to the complications concerning changes in the placement of the optical components, it was never used. All of the measurements were done at room temperature, and the holder was used mainly as a temperature readout.

3.2 Measurement preparation

For possible reproduction of the measurements conducted during this thesis, an exact description of a standard measurement process will be presented.

Before fitting the sample inside the holder, power calibration was checked. This was done by inserting the S122C photodiode in front of the holder and checking five random values of set power. Suppose the measured value corresponded with the one set in software; the loaded power calibration file was accepted. If they differed, a calibration sweep was conducted as described in the previous text.

At this point, a PCB with the sample was inserted into the sample holder. A multi-ribbon cable was connected to the PCB and the breakout box. BNC cables connecting the breakout box to the multimeters and the source meter were connected according to the bonding diagram for devices that had to be measured. At this point, the device's resistance was tested to find out whether some of the bonds did not loosen during the installation.

The first step after fixing the PCB with the sample in place was the spot size measurement. This process was done as described earlier in this chapter. In order to check the perpendicularity of the sample to the incoming beam, spot size was measured at all four corners of a gold calibration square. If the fitted values of the spot size were all in the range of $\pm 1 \mu m$ of each other, alignment was deemed acceptable. If the spot size differed more than the said value, the angle of the sample was readjusted with the adjustment screws on the Polaris holder. This procedure was then repeated until the results were comparable.

The next step was marking the laser spot position on the camera. This had to be done by burning a small area outside of measured devices on the sample. The burned spot was then marked in the ThorLabs camera software and used as a reference when aligning with measured devices. This process of burning a small spot was chosen mainly because of the long distance to the camera. This long camera arm amplified the small angle of the sample to the incoming laser beam into noticeable deflection (20-30 μm between the reflected beam and the actual position of the laser spot).

The laser spot was then aligned with the measured device on the sample according to this mark in the camera software. This alignment was done using manual jogging of the XYZ ThorLabs stage carrying the sample holder. Servomotors were controlled by the Kinesis K-cube motor controllers KDC 101 from ThorLabs.

The last step before the measurement itself was a short sweep from minimum laser power. This was set up to stop a sweep when a spike in the resistance after the laser pulse reached 1% of the device resistance. Laser pulse was emitted every 15 s with increasing power. This quick sweep gave an indicator of starting laser power for the measurement.

4. Experimental measurements

In this chapter, experimental measurements done in the scope of this thesis will be presented.

In the first section, a general introduction to data evaluation techniques used will be given with an example of the measurement process.

The second section will focus on different static characterization measurements. Different substrates, stoichiometries, thicknesses, and device sizes will be compared according to their amplitude dependencies on the applied laser fluence. Differences between them will be discussed, along with different effects that are affecting their quench switching performance.

The last section focuses on positional measurements. Two types of movement were introduced in the measurements. Linear sweeps will be presented in order to characterize the writing region of a laser spot, while the mapping experiment will show the positional dependency of measured amplitude. A measured map will be supplemented by numeric simulation.

4.1 Quench switching induced by optical excitation

Optically induced quench switching exhibits all aspects of electrically induced quench switching described in section 1.5. This work is focused on the normal component of relaxation, which is the most prominent at room temperature, where all of the presented measurements were performed.

During all measurements, devices were read electrically as described in section 3.1.4. Data from all measurement instruments were organized into two files. The first file contained information about the sourced voltage and current, hall probe voltages, and temperature of the sample with their respective time index. The second file included timestamps and intensity of each pulse, along with the laser spot position relative to the start of the measurement.

After importing the data files, four-point resistance was calculated from the measured voltage and current values. Data were cut into chunks after each pulse; one of these chunks is shown in figure 4.1. This allowed individual processing of the behavior during the relaxation period of 100 s.

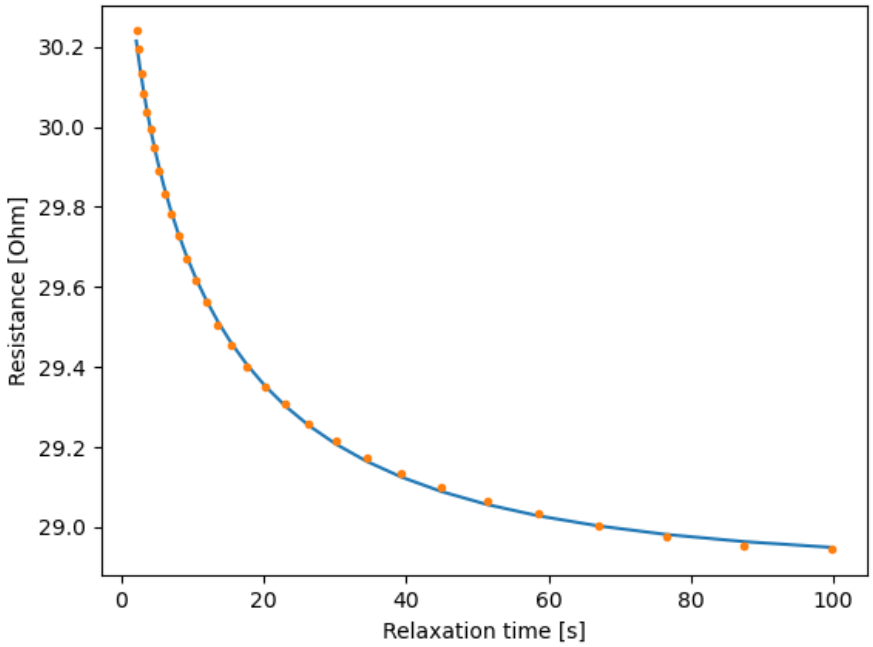

Figure 4.1: Example of the resistance relaxation behaviour after laser pulse excitation. Blue line represents fitted relaxation of stretched exponential function.

Example behavior of the normal component and its relaxation are shown in figure 4.1. Orange dots represent experimental data, which was binned and averaged on a logarithmic scale. This binning is a part of the data processing, which improves the reliability of the fit shown as a blue line. More averaged points towards the end of the relaxation decrease impact of the random fluctuations. In contrast, dense data points at the relaxation beginning offer relevant information for fitting the exponential decay.

Fitting was done using a scipy's library curve-fit function with a stretched exponential function (equation 1.11) in two rounds. In the first round, only relaxation time was fitted, and all the fitted relaxation times with errors smaller than the set error limit were clustered using 1D k-means clustering. Their centroid was used as a relaxation time for the second round of amplitude fitting, which gave the exact amplitude of the switching signal. These amplitudes were then binned according to the intensity of the excitation pulse and then averaged.

All averaged amplitudes were analyzed as absolute values and relative values in relation to the relaxed resistance of the measured device. After 100 s relaxation at room temperature, the last point was taken as a relaxed resistance of the device.

4.2 Amplitude response characterization

With the laser spot aligned and measurement prepared following the steps discussed in section 3.2 a standardized laser intensity sweep in the up-down pattern was employed to characterize the amplitude response. An example of the raw data with an up-down pattern of laser pulses is shown in figure 4.2. The up-down pattern of the laser intensity stepping enables evaluation of the role of laser-induced changes occurring for high fluences.

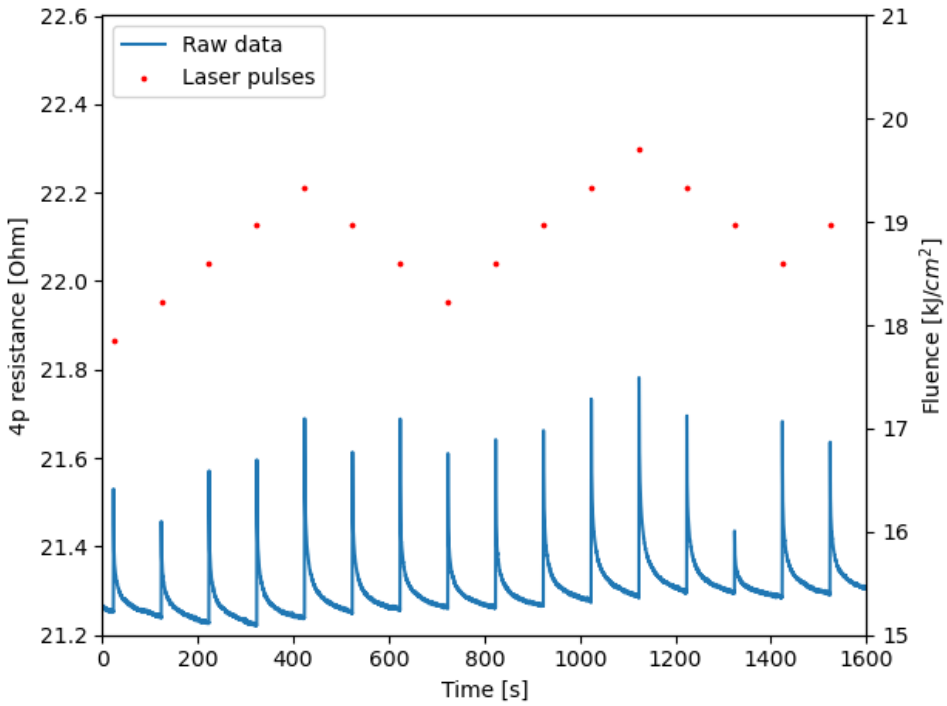

Figure 4.2: Example of 4-point resistance calculated from raw data (blue) with incoming laser pulses (red) in an up-down fluence pattern.

Different comparisons will be derived from the amplitude dependence on the laser fluence (intensity) in the following subsections. Experimental conditions were matched as closely as possible between different samples.

4.2.1 Substrate comparison

A comparison of the amplitude response between 50 nm thin CuMnAs films grown on different substrates will be explored in the following text. For this comparison, three substrate materials were used - GaP, GaAs, and Si. For evaluating the signal response for CuMnAs on each substrate, the signal amplitude dependence on the laser fluence is shown first.

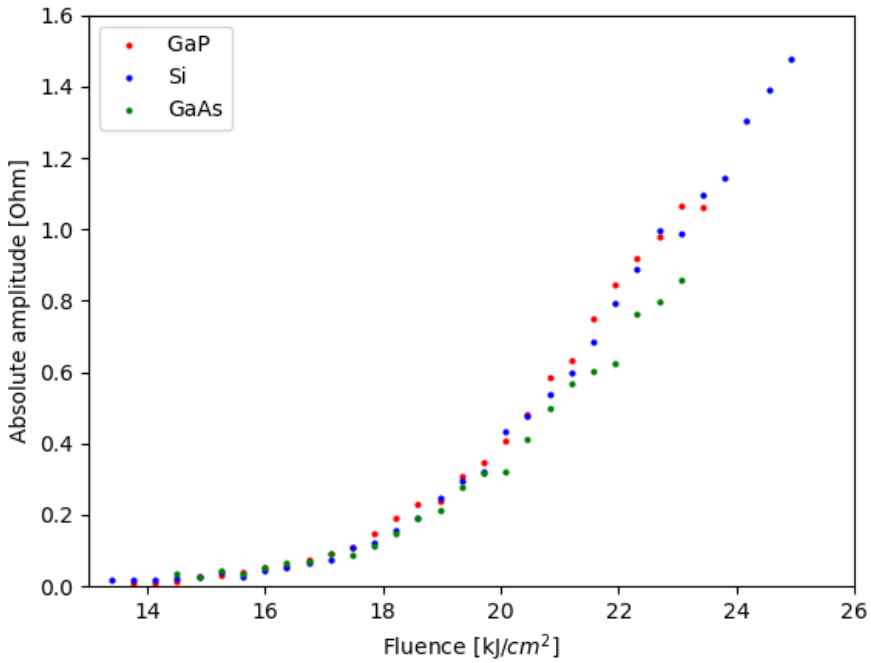

Figure 4.3: Comparison of the average absolute amplitude response of 20 μm devices for 50 nm CuMnAs film grown on different substrates.

Resistance of the device is given by multiple contributions from different effects. These effects are connected to the different scattering mechanisms in metals, and the total resistivity of metal can be written as empirical Matthiessen rule:

$$\rho = \rho_{0i} + \rho(T) + \rho_M \tag{4.1}$$

where ρ_{0i} is a contribution of the lattice impurities, $\rho(T)$ is a temperature-dependent part representing lattice vibration, and ρ_M is an addition to the resistivity from magnetism. As shown in section 1.6, the heat from the CuMnAs film is dissipated within a few ns after the laser pulse; therefore, it is not important on the 100 s timescale of recorded data. The signal is attributed to the magnetic disorder, which is identified by the characteristic relaxation time of around 7.5 s at room temperature. A permanent increase in resistivity is observed for high laser fluences, which is attributed to the change in the material. Therefore in the case of lower laser fluences, evaluating the absolute amplitude is suitable for quantifying the changes in magnetic order. At the same time, evaluation of the relaxed resistance gives insight into the structural damage on the devices.

Data shown in figure 4.3 show that the quench switching effect is equally effective on CuMnAs films of the same thickness grown on different substrates.

At the same time, devices have different base resistance as shown in figure 4.5; hence the quench switching evaluated in relative units shows significant variation. This evaluation favors GaP substrate thanks to the low base resistance of the CuMnAs film grown on it. This low resistance is partly caused by the highest quality of growth and a low number of defects.

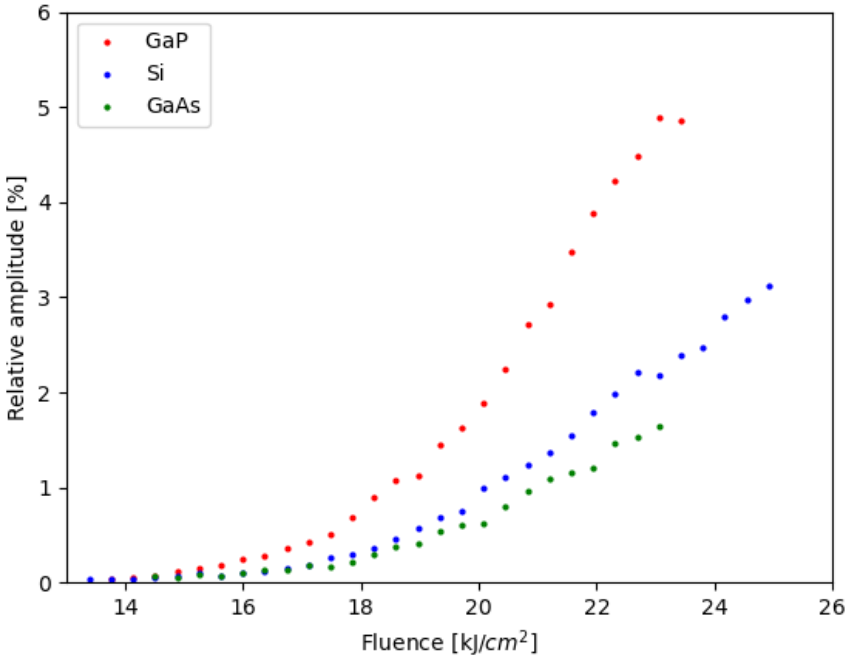

Figure 4.4: Comparison of the average relative amplitude response of 20 μm devices for 50 nm CuMnAs film grown on different substrates.

The evolution of the relaxed resistance of the samples can be seen in figure 4.5. It shows a significant increase in the relaxed resistance of the Si for high laser fluences. This could be explained by the fact that the used wavelength of λ=1030 nm was above the bandgap of Si substrate.

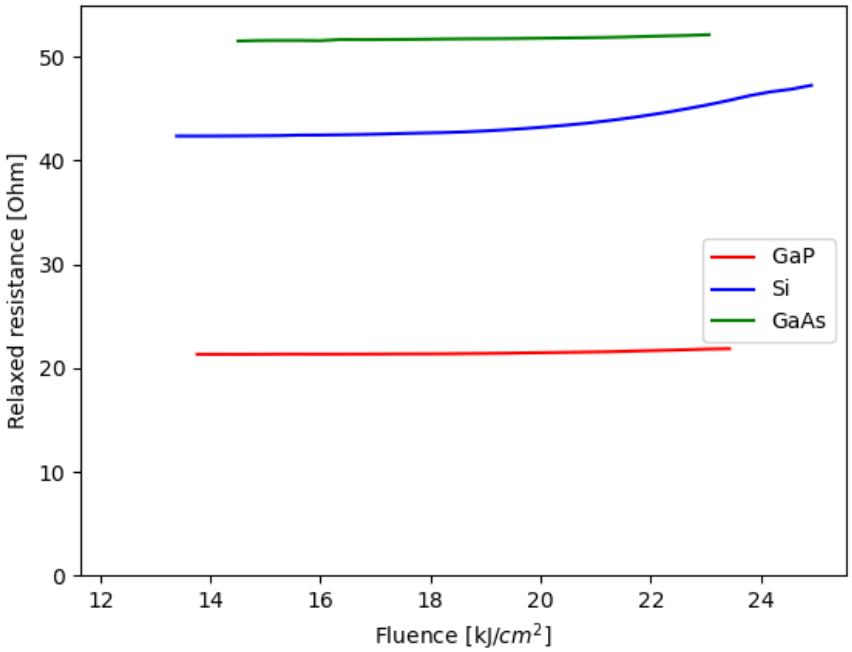

Figure 4.5: Average resistance of the devices after relaxation depending on the laser pulse fluence.

4.2.2 Stoichiometrich and off-stoichiometric CuMnAs comparison

In this subsection, off-stoichiometric CuMnAs films grown on GaP substrate will be compared to their stoichiometric counterpart. As mentioned in section 2.1 CuMnAs films can be prepared with different stoichiometric ratios, thanks to precise control of the molecular fluxes in the MBE. As shown in the previous section, films grown on GaP substrate show the lowest number of defects and highest overall quality, which resulted in their choice.

Three wafers were selected. These wafers were 10% Mn-rich, stoichiometric and 10% Cu-rich. It is known that diversion from stoichiometric 1:1:1 composition of CuMnAs results in the worse electrical switching response [2]. This comparison was not explored with optical excitation before, which motivated this work.

The absolute amplitude data can be compared to the measurements done electrically shown in [2]. Both types of measurements - electrical and this optical excitation shows similar trends. From results shown in figure 4.6 it can be concluded that the perfect 1:1:1 stoichiometric composition of CuMnAs exhibits the best amplitude response of the normal relaxation component. Both Mn-rich and Cu-rich samples have worse amplitude response.

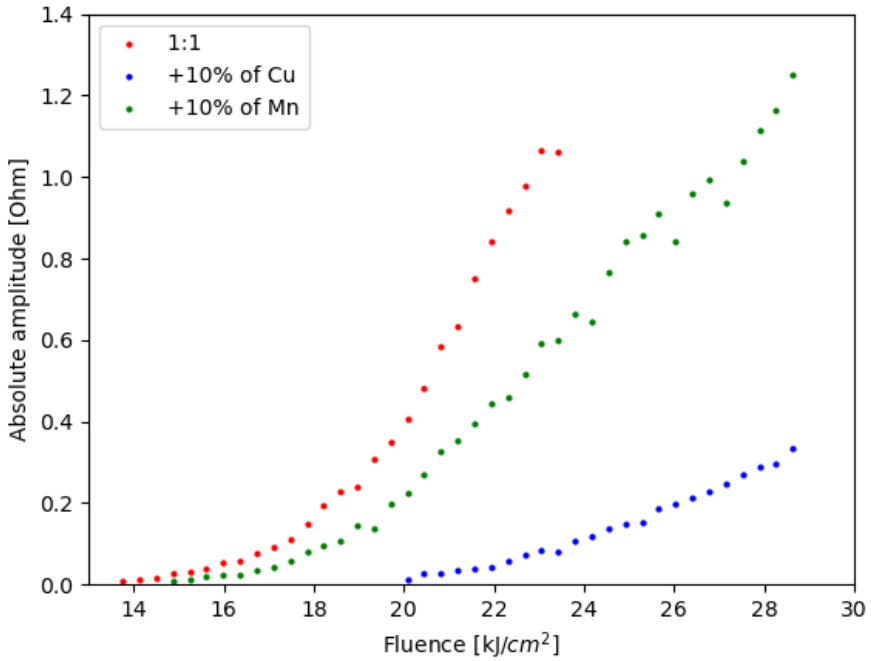

Figure 4.6: Comparison of the average absolute amplitude response of 20 μm devices on 50 nm CuMnAs film grown with different stoichiometries.

Shown data is also consistent with a better response of the Mn-rich sample than the Cu-rich one measured electrically. One surprising result is the much worse amplitude response of the Cu-rich sample, which measured electrically was only slightly worse than the Mn-rich sample. The optical excitation performance of the Cu-rich sample exhibits a ratio of 0.09:1 compared to the stoichiometric sample, which is much lower than what was measured electrically.

Thanks to the relative amplitude dependence shown in figure 4.7 quality of the grown film can be determined. The base resistance of the stoichiometric sample was 21.3 Ohm, Mn-rich had 27 Ohm, and Cu-rich had 23.5 Ohm. Thanks to the higher resistance of the off-stoichiometric samples, further separation from the stoichiometric one can be seen in the relative amplitude plot.

One possible explanation of the bad performance of the Cu-rich sample can be given when looking into the growth behavior of the off-stoichiometric samples. CuMnAs tends to grow with perfect stoichiometry. Therefore, during the over-pressure of Cu, it tends to create local islands with high Cu concentration while keeping the perfect stoichiometry elsewhere. These Cu-rich islands are pushed towards the surface. Measurements done with optical excitation are more sensitive to the surface quality of the samples compared to the electrical ones. Cu islands on the sample's surface can be the reason behind the higher laser fluence needed to start quenching the sample. Their effect on the absorbance of the sample can also lead to a weaker amplitude response.

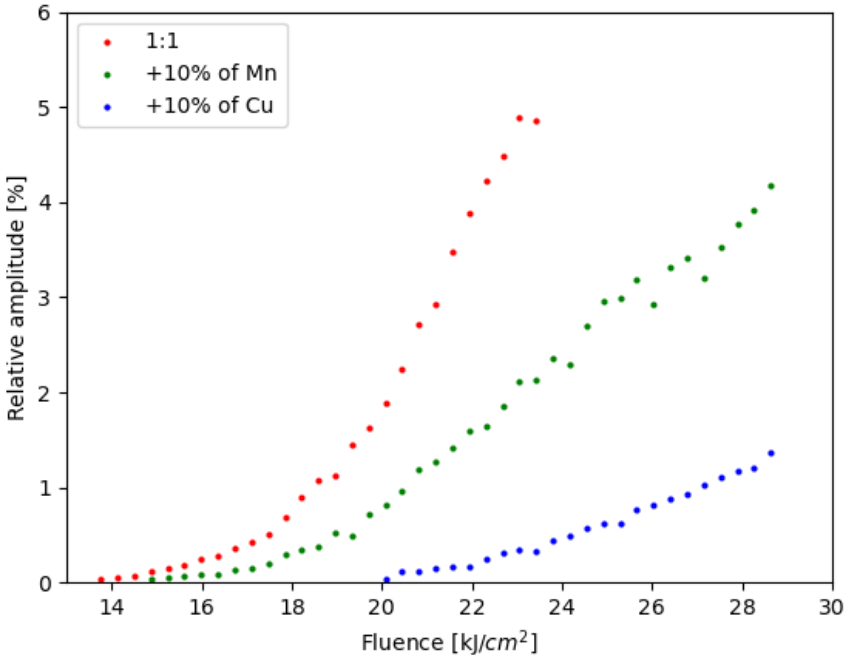

Figure 4.7: Comparison of the average relative amplitude response of 20 μm devices on 50 nm CuMnAs film grown with different stoichiometries.

4.2.3 CuMnAs film thickness comparison

Comparing the 50 nm substrates shown in section 4.2.1 to the ones with 20 nm thin CuMnAs film shows significant differences. These differences stem from the film quality, which varies widely for the thinner CuMnAs films on different substrates [3]. These variations separate compared substrates more from each other and favor the GaP substrate in both absolute amplitude shown in figure 4.8 and relative amplitude shown in figure 4.9. The good quality of the 20 nm CuMnAs film on GaP is supported by its lower base resistance (82.5 Ohm) compared to the films on Si (123 Ohm) and GaAs (171 Ohm) substrates.

The shape of the 20 nm CuMnAs film on GaAs amplitude dependence is probably caused by the strong inhomogeneity of thin CuMnAs films on GaAs. For thicknesses around 10-20 nm, CuMnAs tends to form elongated islands on the GaAs substrate, resulting in strong anisotropy. In thicker films, like 50 nm, those islands are already interconnected into one seamless layer. This behavior is responsible for the very high base resistance of the device (171 Ohm); thus, lower conductivity resulting in a smaller absorption coefficient is seen on GaAs. Smaller anisotropy of CuMnAs film on Si results in base resistance of 123 Ohm slots its onset between GaAs and GaP substrate.

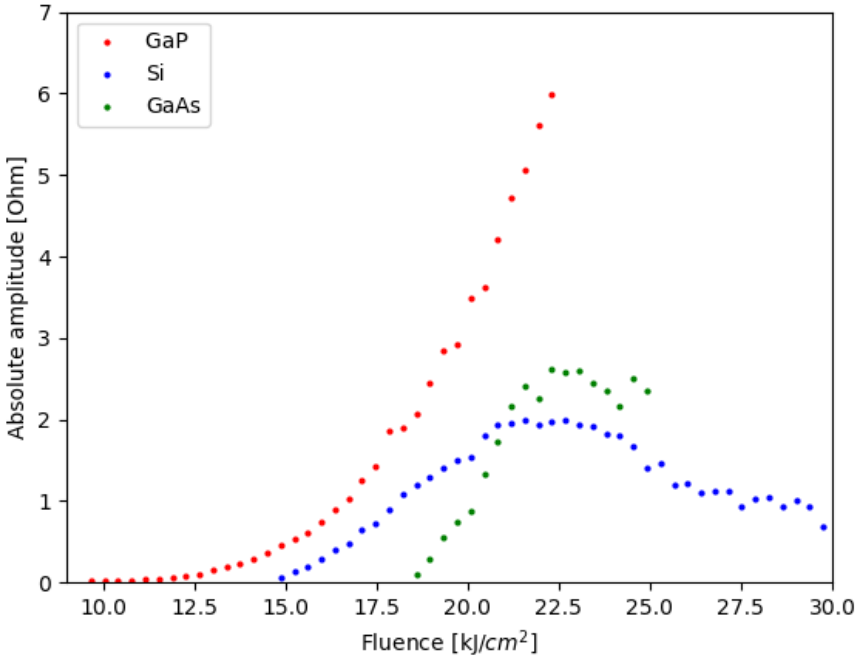

Figure 4.8: Comparison of the average absolute amplitude response of 20 μm devices for 20 nm CuMnAs film grown on different substrates.

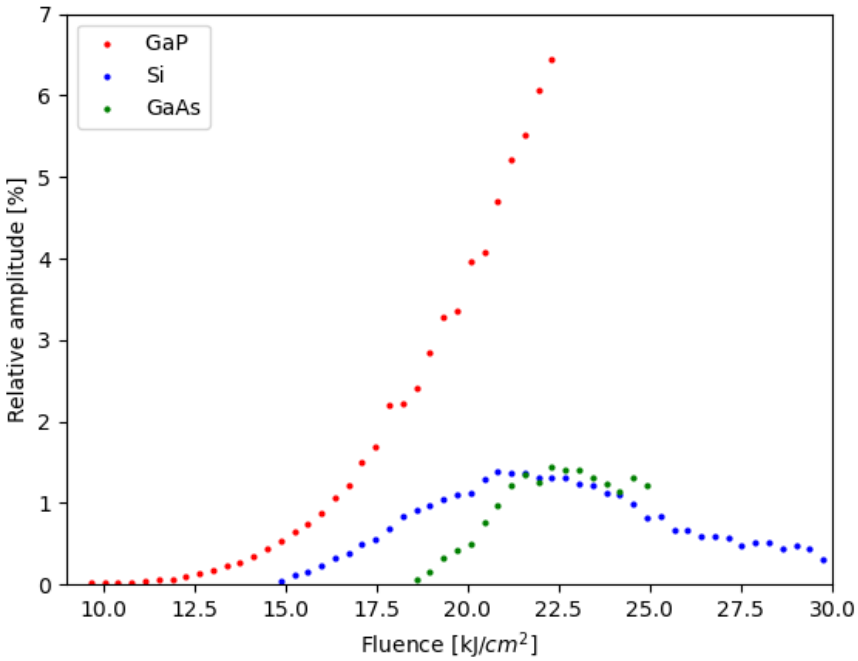

Figure 4.9: Comparison of the average relative amplitude response of 20 μm devices for 20 nm CuMnAs film grown on different substrates.

The rise in relaxed resistivities for higher laser fluence can be seen in figure 4.10. This rise points out significant structural changes in CuMnAs on Si and

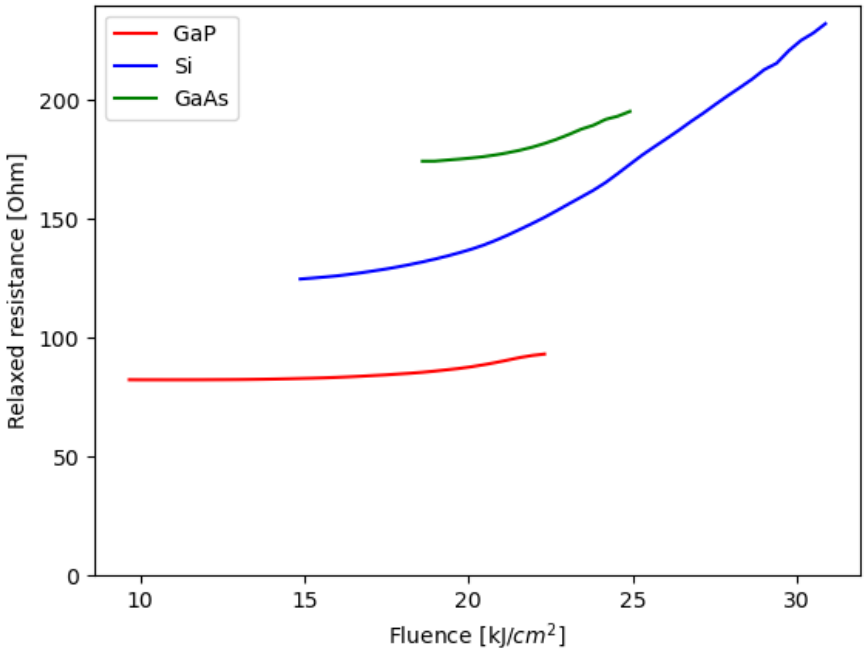

Figure 4.10: Comparison of the average relative amplitude response of 20 μm devices for 20 nm CuMnAs film grown on different substrates.

GaAs substrates. As mentioned previously, the biggest changes can be seen for films on Si substrates, probably because of the used laser wavelength inside the bandgap of Si.

This worse performance of the 20nm CuMnAs on Si and GaAs was the reason why GaP substrates were chosen for direct thickness comparison, which should answer which film thickness produces a higher relative amplitude of quench switching. Choice of the relative amplitude was taken to normalize the results to the higher base resistance of the 20 nm thin film. As mentioned in 1.6, the temperature of the CuMnAs film decreases with depth; only a small part is heated above the Neél temperature. Decreasing the thickness of the film increases the cross-sectional ratio between quenched and not quenched parts of the CuMnAs. This manifests itself in the steeper rise of the initial amplitude signal observed for the 20 nm CuMnAs film shown in figure 4.11.

Results show a sooner rise in relative amplitude depending on the laser fluence. Spot size and size of the device are the same in this comparison. As mentioned above ratio of the quenched region to the unaffected CuMnAs is higher in the thinner film; thus, the higher relative amplitude is achieved for the same laser fluence compared to the thicker film.

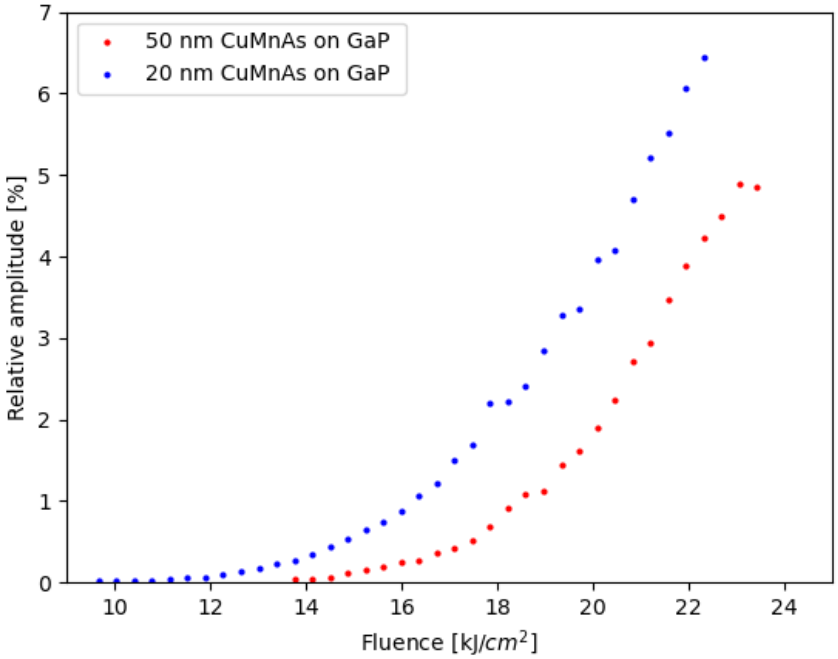

Figure 4.11: Comparison of relative amplitude dependence for 20 nm and 50 nm thick CuMnAs film on GaP substrate.

4.2.4 Comparison of different sized devices

Evaluating the dependence of the amplitude signal on the size ratio between the active area of the device and laser spot was done using two different sized devices - standard 20 μm and smaller 10 μm one. The laser spot size was the same during the experiments, and both one square devices were on the same sample; therefore, the only different parameter was their size.

The samples chosen for this comparison were 50 nm and 20 nm CuMnAs films on GaP, thanks to their consistent behavior described earlier.

Thanks to the same spot size for both measurements, the 10 μm square was exposed to a higher and more homogeneous energy density than the 20 μm square for the same laser fluence. This resulted in a steeper rise of the amplitudes with increasing laser fluence. This is supported by data shown in figure 4.12, which show the onset at the same fluence, marking the quenching threshold, while 10 μm device shows a significantly steeper trend.

In figure 4.13 effects of higher energy density to the active area show sooner manifestation of the burning effect as saturation of the amplitude on a smaller device. Even though the absolute amplitude was still rising, relative amplitude shows this burning clearly from the laser fluence of 21 kJ/cm^2.

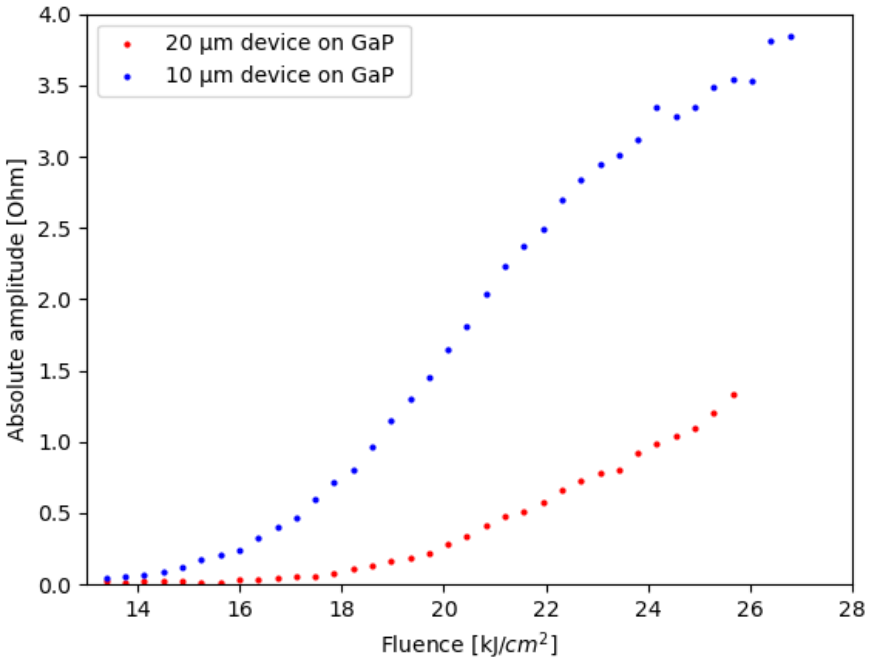

Figure 4.12: Comparison of the absolute average amplitude dependence for 10 μm and 20 μm single square devices on 50 nm CuMnAs film on GaP.

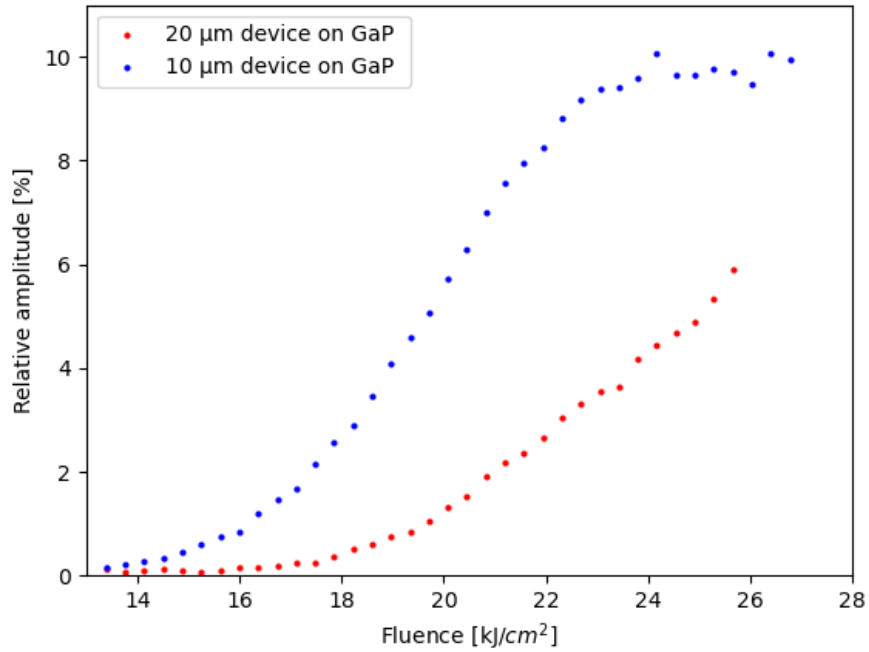

Figure 4.13: Comparison of the relative average amplitude dependence for 10 μm and 20 μm single square devices on 50 nm CuMnAs film on GaP.

20 nm CuMnAs film offers a significant increase in separation between the 10 and 20 μm devices shown in figure 4.14. Although it might seem like 20 μm

device underperformed, when the scale of the graph is taken into account, its performance is on par with devices shown in section 4.2.3. The steep rise in amplitude of the $10\mu m$ is a combination of both higher energy in relation to the device's active area and the steeper response of thinner films.

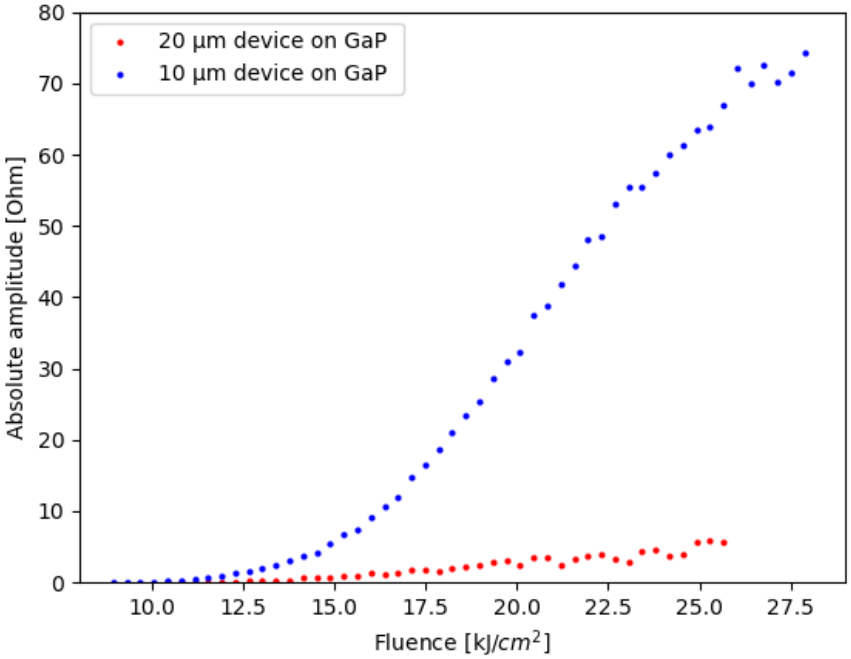

Figure 4.14: Comparison of the absolute average amplitude dependence for 10 μm and 20 μm single square devices on 20 nm CuMnAs film on GaP.

Even though the relative amplitude shown in figure 4.15 shows burning for fluence above 20 kJ/cm^2, the absolute amplitude is still rising, which can be seen when comparing with figure 4.14. This manifests how the geometry of the device is changing with burning. As impurities are introduced due to these structural changes in the center of the device, the current path changes significantly, transforming it from a single square device into two parallel multi square devices. Lower laser intensities on the edges of the laser spot are still switching these new devices, which results in the increasing absolute amplitude. At the same time, structural changes manifest themselves in the relative amplitude.

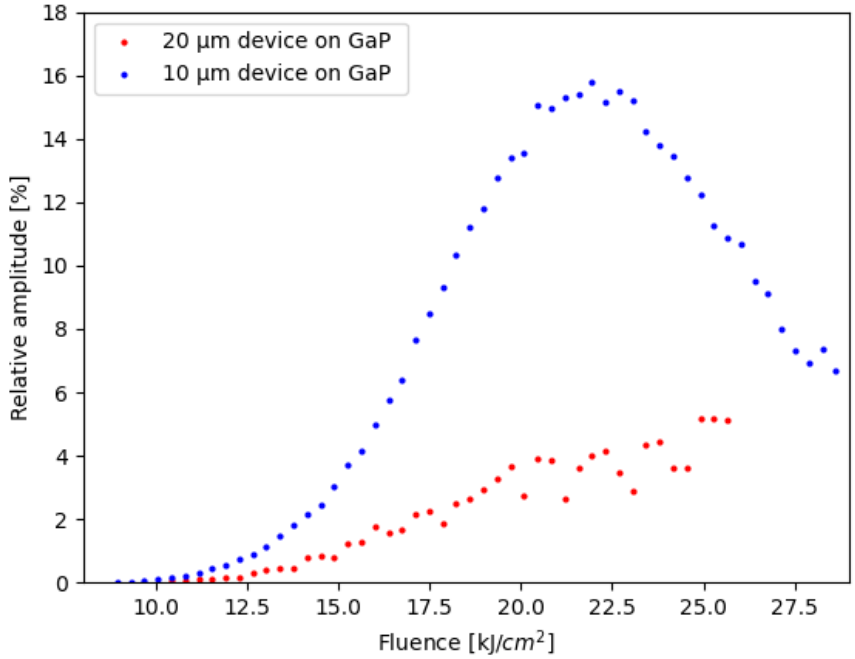

Figure 4.15: Comparison of the relative average amplitude dependence for 10 μm and 20 μm single square devices on 20 nm CuMnAs film on GaP.

4.3 Positional measurements

Positional measurements were done on the double square hallbar described in section 2.3 which allowed independent measurement of both squares. Each square was connected to one multimeter, and they were sourced along the same path as shown in figure 2.8.

Two types of positional measurements were done. The first one consisted of a single scanning pass on the axis of the device. The geometry of this measurement is shown in figure 4.16a. Green points represent individual positions of the laser beam, which itself is illustrated with a red gaussian profile. At each of the positions spaced by 2 μm, a single laser pulse was emitted, and 100 s relaxation was allowed before changing the position. This whole sweep was repeated for four different laser fluences.

The second measurement aimed to create a map of amplitude dependency. Mapped positions are shown in figure 4.16b, similarly to the previous measurement. In this measurement, positions were spaced by 3 μm, and the whole map was done only using one laser fluence, which was selected to produce a reasonable amplitude signal.

4.3.1 Laser spot writing region

The intensity profile of a Gaussian beam is shown in figure 3.4. Because the quench switching effect only occurs when the local temperature is higher than the Neél temperature, only a small central part of the laser spot causes the quench switching effect—this area above the threshold increases with increasing

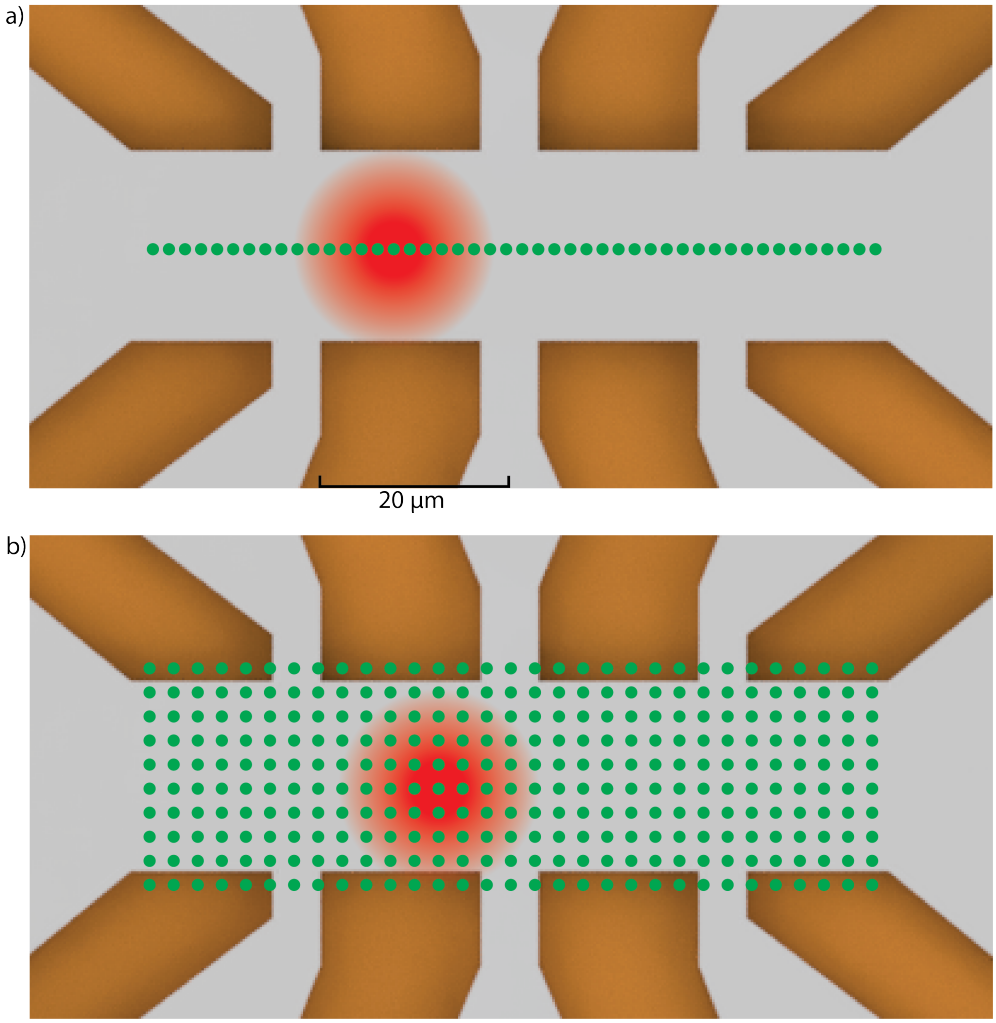

Figure 4.16: Representation of the positional measurements on double square hallbars. a) Single pass measurement. Green dots represent individual positions of a laser spot (shown in red). b) Mapping measurement.

laser power.

One of the goals of this thesis was to determine the evolution of the switched area with increasing laser power. The experiment aimed at measuring the writing area was done on the double-hallbar device. Detailed description can be found in the introduction of this section.

An example of measured data from this experiment is shown in figure 4.17. The top two graphs show resistance of left and right square respectively. In the bottom one, absolute amplitude values with their positional value are shown along with the Gaussian functions used for their fitting.

Amplitude dependencies for all measured intensities were fitted in the same way. These fits are shown in figure 4.18. The writing region was evaluated by surpassing a threshold value of 0.05 Ohm.

Results of this evaluation can be found in table 4.1. Estimated writing region was determined from the average distance between intersections of Gaussian fit and threshold, from which width of measured square (20 μm) was subtracted.

This analysis quantifies the qualitative observation that a larger area of the

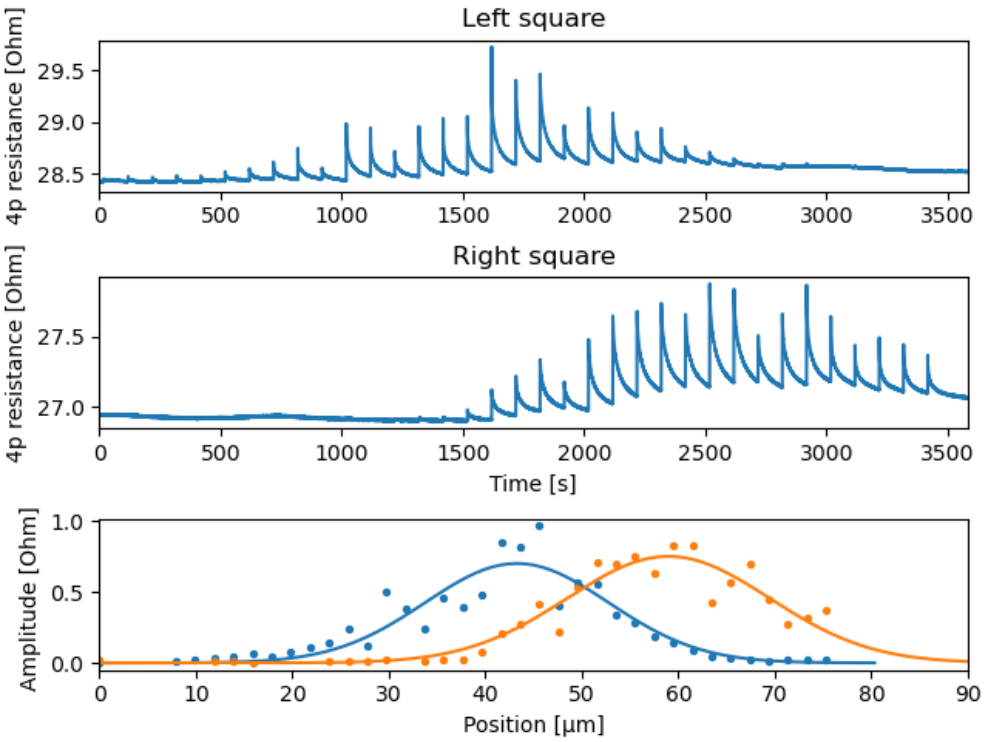

Figure 4.17: Example of laser spot writing region measurement for 60 mW laser intensity. Left and right square 4point resistance data is shown on the first two graphs. The bottom one shows amplitudes with their respective position and fitted Gaussian functions.

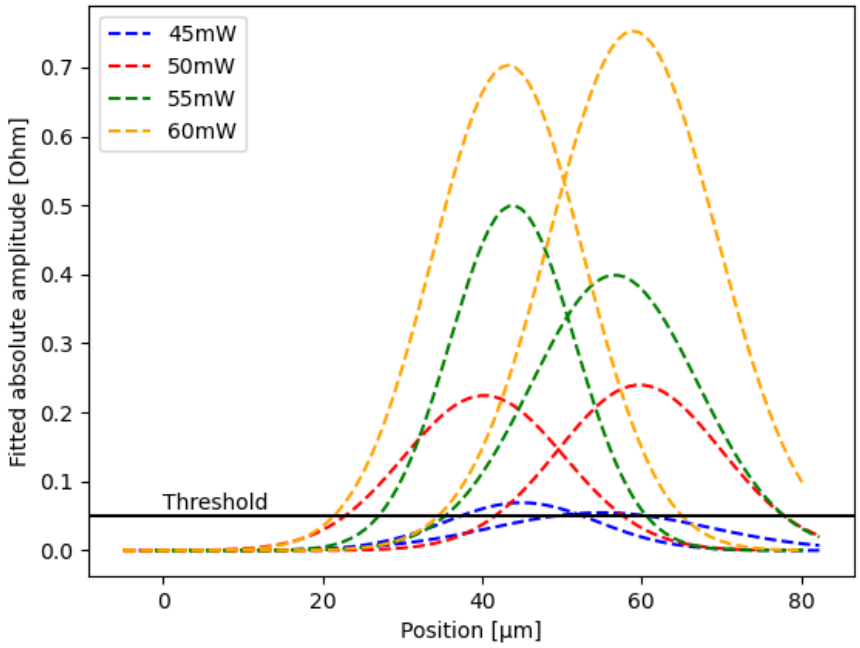

Figure 4.18: Fitted Gaussian function dependencies of amplitudes on position for different laser intensities.

Table 4.1: Writing spot evaluation.

Laser intensity [mW]	Laser fluence $[kJ/cm^2]$	Intersection spacing $[\mu m]$	Estimated writing spot diameter $[\mu m]$
45	16.74	13	NaN
50	18.60	35	15
55	20.46	38	18
60	22.31	46	25

device is quenched into the high resistive state with increasing intensity. A larger area also reflects in a larger measured amplitude. The laser spot profile was the same in all measurements. The only changed variable was the intensity; therefore, the written region's change depends only on the laser intensity.

4.3.2 Amplitude map

The creation of the amplitude map will be explored in this subsection. As mentioned above, laser pulses of the same intensity (50mW) were aimed at different positions on the hallbar. A 100 s interval temporally spaced them to allow sufficient relaxation at each pulsed position. These relaxations were then fitted with the exponential relaxation equation 1.11. Maps shown in figure 4.19 were processed with a script provided by Mgr. Miloš Surýnek and were adapted to overlay a model of a double square device.

These maps suggest one exciting phenomenon. This phenomenon is the negative amplitude of a normal relaxation component seen just outside the measured square (blue regions). This is not a negative component normally found in electrical quench switching of CuMnAs, because the characteristic relaxation time is the same as for the normal component. In contrast, the negative component seen electrically exhibits one order of magnitude shorter relaxation time. In this case, the negative component results from a change in the path of the electrical current. This change is caused by quench switching a spot with a few μm and creating this inhomogeneity with higher resistivity than the rest of the hallbar. When this inhomogeneity is close to the measurement contact, current flows around it and creates an area with lower current density behind it. This change in current flow manifests as a decrease in the voltage measured between the hall probes.

This behavior is further supported by the simulations, which were done using the software Comsol Multiphysics. In these simulations, inhomogeneity with higher resistance to the rest of the device was placed in different locations, and voltage on the hall probes was evaluated. The simulation was done for a stationary case, and no relaxation was introduced to the inhomogeneity. The resulting images can be found in figure 4.20 and similarity to the measured data is seen.

Another important piece of information from these maps is the information about the positional sensitivity of all measurements conducted during this thesis. As is clearly visible in figure 4.19 measured amplitude is strongly dependent on the position of the laser spot. This dependency suggests the necessity of a precise positioning system with good mechanical stability. This was not the case in these measurements because the used XYZ motorized stage from Thorlabs experienced random wobble of around 3 μm, which persisted throughout all measurements.

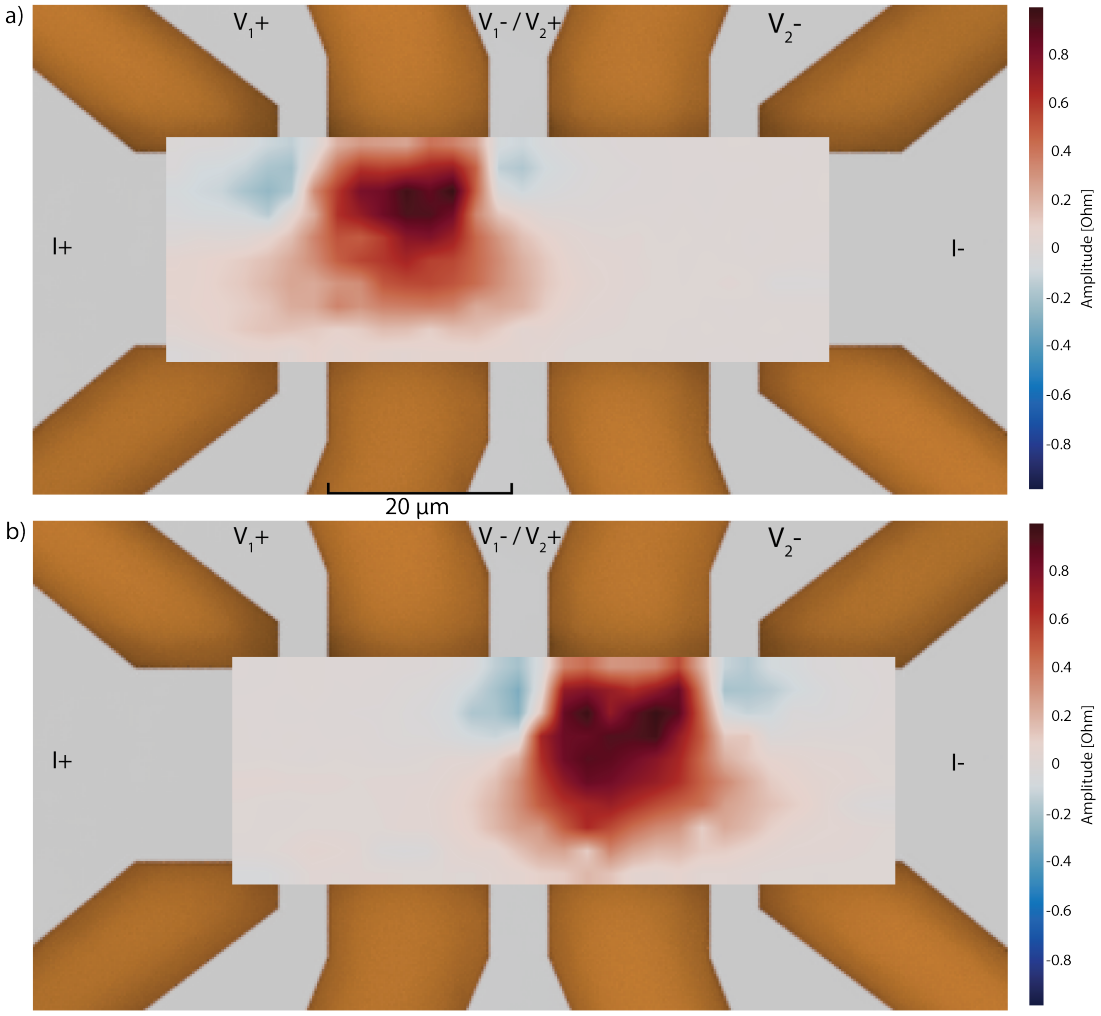

Figure 4.19: Measured maps showing positional amplitude dependence layed over the modeled device. a) Amplitutdes from left square measurements. b) Amplitutdes from right square measurements.

This wobble is an inherent side-effect of the spring-loaded mechanical stage. Minor imperfections in the ball of a motor-controlled pushrod or meeting surface on stage are causes of this wobble. Another culprit is the springs themselves, or more exactly, temperature-induced changes in them. Their stress relief causes small movements, which correspond to wobbly behavior.

These issues discovered with this measurement will be fixed in the future by replacing the XYZ stage with a closed-loop magnetic drive system. This is an intermediate system between the piezo positioning system and a more classic stepper motor system. Magnetic drives have piezo-like stepping (up to 20 nm per step) and stepper motor-like travel ranges (more than 50mm). These attributes combined with closed-loop control make them the best candidate to replace the currently used XYZ stage.

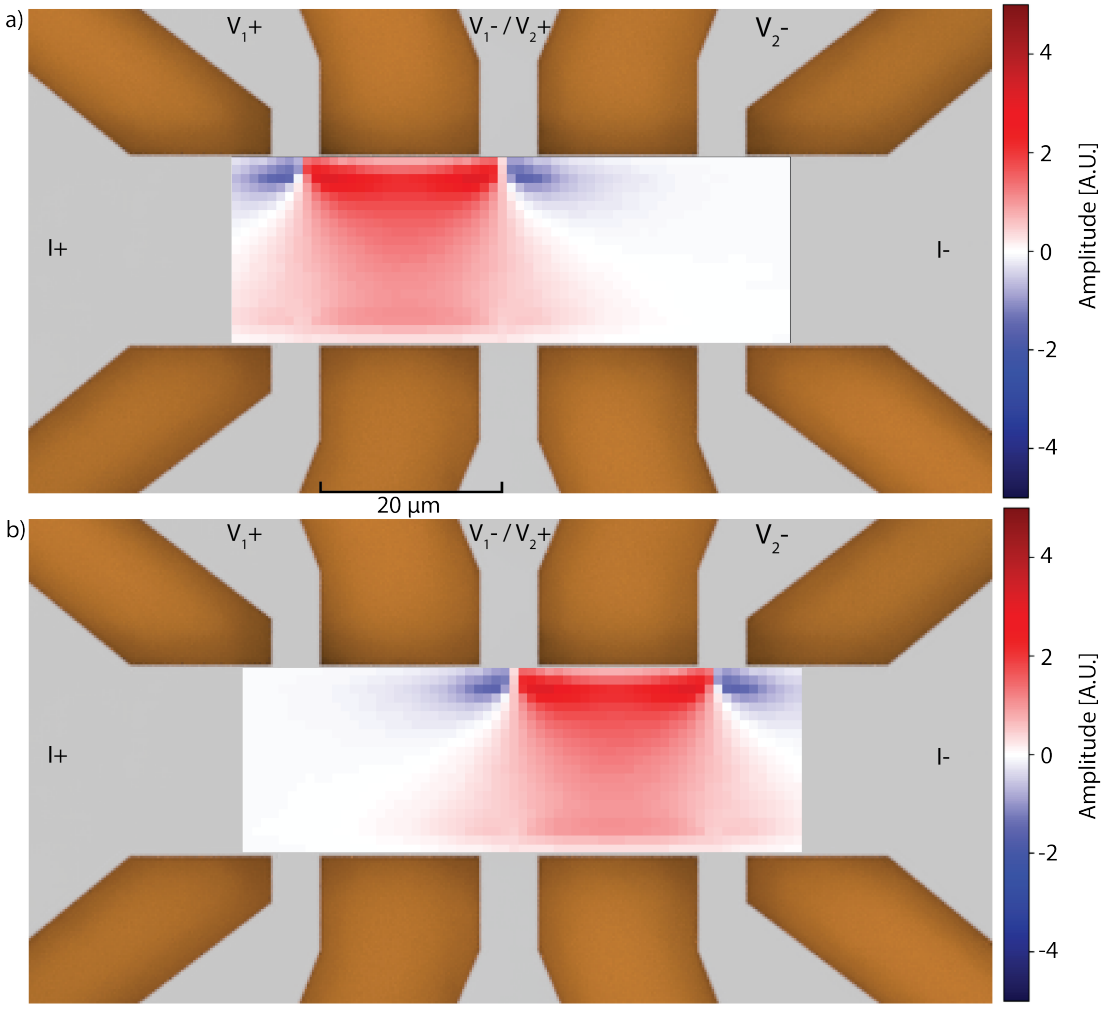

Figure 4.20: Simulated maps showing positional amplitude dependence layed over the modeled device. a) Amplitutdes from left square. b) Amplitutdes from right square.

Conclusion

A comprehensive study of the Quench switching effect in antiferromagnetic CuMnAs films using optical excitation was presented in this thesis. Resistivity changes caused by the quench switching were evaluated for different substrate materials, stoichiometries, CuMnAs film thicknesses, and device sizes. Moreover, positional dependencies were studied, which provided information on the laser spot writing region and positional dependency of the measured change in resistivity. This evaluation provided a useful guide for improving the CuMnAs response using excitation by a single 120 fs laser pulse.

In the case of the substrate comparison for 50 nm CuMnAs films, the absolute amplitude response of the quench switching is comparable between all substrates. This indicates that the magnetic disorder induced by quench switching is very similar for all 50 nm films. The relative amplitude response favors CuMnAs on GaP substrate thanks to its higher growth quality and, therefore, lower base resistance.

Comparison of different CuMnAs stoichiometries was made for films grown on GaP substrate. Stoichiometric samples show the best response to the optical excitation. Worse response of the off-stoichiometric samples is probably connected to their lower surface quality, which stems from the formation of islands on the surface made up of excess elements. These islands can change the optical properties of CuMnAs film.

The need for the good surface quality of the CuMnAs is further emphasized by looking at 20 nm CuMnAs films on GaP, GaAs, and Si substrates. In this comparison, film grown on GaP has the best all-around attributes, thanks to its good growth quality even for thin layers, which is not the case for GaAs and Si substrates. A direct comparison of 20 nm and 50 nm thick films of CuMnAs favors the thinner films for their higher cross-sectional ratio of quench switched region. This can be attributed to the exponential decay of laser intensity in the CuMnAs film's cross-section; only the hottest part below the surface is excited above the Neél temperature and, in turn, quench switched.

Comparison of different sizes of the devices with regard to the size of the laser shows higher amplitudes for the smaller devices. This stems from the usage of laser spot with fixed size and Gaussian profile during the measurements. When the device's active area is small, it experiences higher and more homogeneous energy density. Therefore a larger part of the active area is brought above the quenching threshold.

The effective area of the laser spot was analyzed from measurements with introduced linear movement across the sensitive part of the device. With increasing laser intensity, the diameter of its effective area increases for fixed spot size, as the larger part of the Gaussian profile reaches above the threshold intensity for the quench switching.

The last measurement presented was the positional amplitude dependence, which showed the best alignment of the laser spot on the device. It also showed an inversion of the signal for places just outside of the measured area of the hallbar. This inversion was also seen in simulated data, and it originates from the introduction of a higher resistance spot, which then prompts a change in the current path in the device.

An important side-effect of optical excitation seen in the measurements is the damage of the film's surface. This damage manifests as an increase in the relaxed resistance of the device. With increasing laser intensity needed to excite a larger area of the device, the intensity in the center surpasses the damage threshold.

The damage caused by the high intensity of the exciting laser pulse differs from the damage caused by electrical excitation. Both manifest as an increase in relaxed resistance; however, their evolution is different. In the case of the optical pulses, the damaged area slowly spreads in both vertical and horizontal directions with the increasing laser intensity. Therefore, only a part of the cross-section of the device is damaged. In contrast, when the electrical current pulses exceed the damage threshold, the damage occurs in the whole cross-section of the device, resulting in faster deterioration. Moreover, the rise of the resistance of the damaged part of the device then leads to more heating during the subsequent electrical pulses, which accelerates the damage even more.

From the measurements done in this thesis, it can be concluded that to optimize the response of the CuMnAs film, the laser pulse with homogeneous intensity between the quenching and the damage thresholds is needed.

Planned usage of a flat-top beam shaper can produce a square-like intensity profile of the laser beam. Switching from the Gaussian distribution to this square-like intensity profile will eliminate the overheated center of the device. A significant drawback of usage of such beam shaper lies in need to rebuild the whole optical setup since the flat-top mode is not a free space mode of light.

A map created during the experiments showed the positional sensitivity of the quench switching. In order to explore it with a better resolution, a change to a more stable XYZ platform is needed. The open-loop servo-driven stage is planned to be replaced by the closed-loop magnetic drives, with repeatability of just 100 nm. The next planned change is the encasement of the sample space in the dry-air enclosure, which will allow using the cooling capability of the sample holder constructed during this thesis. When these changes to the setup are complete, multiple experiments are planned. First of which focuses on the other components of the switching, which can be studied at different temperatures. Another experiment combines the precise movement of the writing spot with cooling, which prolongs the relaxation. In this experiment, we plan to manipulate the current path along the device by patterns defined with quench switched regions of the device.

Bibliography

[1] Zdenek Kaspar, M. Surýnek, Jan Zubáč, Filip Krizek, Vit Novak, Richard Campion, Martin Wörnle, P. Gambardella, X. Marti, P. Němec, Kevin Edmonds, S. Reimers, Oliver Amin, F. Maccherozzi, S. Dhesi, Peter Wadley, J. Wunderlich, Kamil Olejnik, and T. Jungwirth. Quenching of an antiferromagnet into high resistivity states using electrical or ultrashort optical pulses. *Nature Electronics*, 4:1–8, 01 2021.

[2] Zdenek Kaspar. *Quench Switching of Antiferromagnetic CuMnAs*. PhD thesis, Institute of Physics of the Czech Academy of Sciences, 2021.

[3] Filip Krizek, Zden ěk Kašpar, Aliaksei Vetushka, Dominik Kriegner, Elisabetta M. Fiordaliso, Jan Michalicka, Ond řej Man, Jan Zubáč, Martin Brajer, Victoria A. Hills, Kevin W. Edmonds, Peter Wadley, Richard P. Campion, Kamil Olejník, Tomá š Jungwirth, and Vít Novák. Molecular beam epitaxy of cumnas. *Phys. Rev. Materials*, 4:014409, Jan 2020.

[4] S. Blundell. *Magnetism in Condensed Matter*. Oxford Master Series in Condensed Matter Physics. OUP Oxford, 2001.

[5] H.P. Myers. *Introductory Solid State Physics*. CRC Press, 1997.

[6] Louis Néel. Magnetism and local molecular field. *Science*, 174(4013):985–992, 1971.

[7] Charles Kittel. Physical theory of ferromagnetic domains. *Rev. Mod. Phys.*, 21:541–583, Oct 1949.

[8] Ernest Huber, D. Smith, and J. Goodenough. Domain-wall structure in permalloy films. *Journal of Applied Physics*, 29:294–295, 03 1958.

[9] M. Wang, C. Andrews, S. Reimers, O. J. Amin, P. Wadley, R. P. Campion, S. F. Poole, J. Felton, K. W. Edmonds, B. L. Gallagher, A. W. Rushforth, O. Makarovsky, K. Gas, M. Sawicki, D. Kriegner, J. Zubáč, K. Olejník, V. Novák, T. Jungwirth, M. Shahrokhvand, U. Zeitler, S. S. Dhesi, and F. Maccherozzi. Spin flop and crystalline anisotropic magnetoresistance in cumnas. *Phys. Rev. B*, 101:094429, Mar 2020.

[10] T. McGuire and R. Potter. Anisotropic magnetoresistance in ferromagnetic 3d alloys. *IEEE Transactions on Magnetics*, 11(4):1018–1038, 1975.

[11] A. W. Rushforth, K. Výborný, C. S. King, K. W. Edmonds, R. P. Campion, C. T. Foxon, J. Wunderlich, A. C. Irvine, P. Vašek, V. Novák, K. Olejník, Jairo Sinova, T. Jungwirth, and B. L. Gallagher. Anisotropic magnetoresistance components in (ga,mn)as. *Phys. Rev. Lett.*, 99:147207, Oct 2007.

[12] M. Wang, C. Andrews, S. Reimers, O. J. Amin, P. Wadley, R. P. Campion, S. F. Poole, J. Felton, K. W. Edmonds, B. L. Gallagher, A. W. Rushforth, O. Makarovsky, K. Gas, M. Sawicki, D. Kriegner, J. Zubáč, K. Olejník, V. Novák, T. Jungwirth, M. Shahrokhvand, U. Zeitler, S. S. Dhesi, and

F. Maccherozzi. Spin flop and crystalline anisotropic magnetoresistance in cumnas. *Phys. Rev. B*, 101:094429, Mar 2020.

[13] M. N. Baibich, J. M. Broto, A. Fert, F. Nguyen Van Dau, F. Petroff, P. Etienne, G. Creuzet, A. Friederich, and J. Chazelas. Giant magnetoresistance of (001)fe/(001)cr magnetic superlattices. *Phys. Rev. Lett.*, 61:2472–2475, Nov 1988.

[14] R. Schad, C. D. Potter, P. Beliën, G. Verbanck, V. V. Moshchalkov, and Y. Bruynseraede. Giant magnetoresistance in fe/cr superlattices with very thin fe layers. *Applied Physics Letters*, 64(25):3500–3502, 1994.

[15] S. Parkin. Magnetotransport in transition metal multilayered structures. 2006.

[16] J Bass and W.P Pratt. Current-perpendicular (cpp) magnetoresistance in magnetic metallic multilayers. *Journal of Magnetism and Magnetic Materials*, 200(1):274–289, 1999.

[17] Nevill Francis Mott and Ralph Howard Fowler. The electrical conductivity of transition metals. *Proceedings of the Royal Society of London. Series A - Mathematical and Physical Sciences*, 153(880):699–717, 1936.

[18] E.Y. Tsymbal and D.G. Pettifor. *Perspectives of Giant Magnetoresistance published in Solid State Physics*, volume 56. Academic press, 2001.

[19] J. S. Moodera, Lisa R. Kinder, Terrilyn M. Wong, and R. Meservey. Large magnetoresistance at room temperature in ferromagnetic thin film tunnel junctions. *Phys. Rev. Lett.*, 74:3273–3276, Apr 1995.

[20] T. Miyazaki and N. Tezuka. Giant magnetic tunneling effect in fe/al2o3/fe junction. *Journal of Magnetism and Magnetic Materials*, 139(3):L231–L234, 1995.

[21] P. Wadley, V. Novák, R.P. Campion, C. Rinaldi, X. Martí, H. Reichlová, J. Železný, J. Gazquez, M.A. Roldan, M. Varela, D. Khalyavin, S. Langridge, D. Kriegner, F. Máca, J. Mašek, R. Bertacco, V. Holý, A.W. Rushforth, K.W. Edmonds, B.L. Gallagher, C.T. Foxon, J. Wunderlich, and T. Jungwirth. Tetragonal phase of epitaxial room-temperature antiferromagnet CuMnAs. *Nature Communications*, 4(1), August 2013.

[22] D.C. Ralph and M.D. Stiles. Spin transfer torques. *Journal of Magnetism and Magnetic Materials*, 320(7):1190–1216, 2008.

[23] A. H. MacDonald and M. Tsoi. Antiferromagnetic metal spintronics. *Philosophical Transactions of the Royal Society A: Mathematical, Physical and Engineering Sciences*, 369(1948):3098–3114, 2011.

[24] P. Wadley, B. Howells, J. Železný, C. Andrews, V. Hills, R. P. Campion, V. Novák, K. Olejník, F. Maccherozzi, S. S. Dhesi, S. Y. Martin, T. Wagner, J. Wunderlich, F. Freimuth, Y. Mokrousov, J. Kuneš, J. S. Chauhan, M. J. Grzybowski, A. W. Rushforth, K. W. Edmonds, B. L. Gallagher,

and T. Jungwirth. Electrical switching of an antiferromagnet. *Science*, 351(6273):587–590, 2016.

[25] K. Olejník, V. Schuler, X. Marti, V. Novák, Z. Kašpar, P. Wadley, R. P. Campion, K. W. Edmonds, B. L. Gallagher, J. Garces, M. Baumgartner, P. Gambardella, and T. Jungwirth. Antiferromagnetic CuMnAs multi-level memory cell with microelectronic compatibility. *Nature Communications*, 8(1), May 2017.

[26] M. S. Wörnle, P. Welter, Z. Kašpar, K. Olejník, V. Novák, R. P. Campion, P. Wadley, T. Jungwirth, C. L. Degen, and P. Gambardella. Current-induced fragmentation of antiferromagnetic domains, 2019.

[27] R. Kohlrausch. Die elektromotorische kraft ist der elektroskopischen spannung an den polen der geöffneten kette proportional. *Annalen der Physik*, 151(10):220–228, 1848.

[28] P. Wadley, V. Hills, M. R. Shahedkhah, K. W. Edmonds, R. P. Campion, V. Novák, B. Ouladdiaf, D. Khalyavin, S. Langridge, V. Saidl, P. Nemec, A. W. Rushforth, B. L. Gallagher, S. S. Dhesi, F. Maccherozzi, J. Železný, and T. Jungwirth. Antiferromagnetic structure in tetragonal CuMnAs thin films. *Scientific Reports*, 5(1), November 2015.

[29] Peter Wadley, Sonka Reimers, Michal J Grzybowski, Carl Andrews, Mu Wang, Jasbinder S Chauhan, Bryan L Gallagher, Richard P Campion, Kevin W Edmonds, Sarnjeet S Dhesi, Francesco Maccherozzi, Vit Novak, Joerg Wunderlich, and Tomas Jungwirth. Current polarity-dependent manipulation of antiferromagnetic domains. *Nature nanotechnology*, 13(5):362—365, May 2018.

[30] Filip Krizek, Sonka Reimers, Zdeněk Kašpar, Alberto Marmodoro, Jan Michalička, Ondřej Man, Alexander Edstrom, Oliver J. Amin, Kevin W. Edmonds, Richard P. Campion, Francesco Maccherozzi, Sarnjeet S. Dnes, Jan Zubáč, Jakub Železný, Karel Výborný, Kamil Olejník, Vít Novák, Jan Rusz, Juan C. Idrobo, Peter Wadley, and Tomas Jungwirth. Atomically sharp domain walls in an antiferromagnet, 2020.

[31] C.-K. Sun, F. Vallée, L. H. Acioli, E. P. Ippen, and J. G. Fujimoto. Femtosecond-tunable measurement of electron thermalization in gold. *Phys. Rev. B*, 50:15337–15348, Nov 1994.

[32] E. Carpene, E. Mancini, C. Dallera, M. Brenna, E. Puppin, and S. De Silvestri. Dynamics of electron-magnon interaction and ultrafast demagnetization in thin iron films. *Phys. Rev. B*, 78:174422, Nov 2008.

[33] M. Surýnek, V. Saidl, Z. Kašpar, V. Novák, R. P. Campion, P. Wadley, and P. Němec. Investigation of magnetic anisotropy and heat dissipation in thin films of compensated antiferromagnet cumnas by pump–probe experiment. *Journal of Applied Physics*, 127(23):233904, 2020.

[34] V. Novák, K. Olejník, M. Cukr, L. Smrčka, Z. Remeš, and J. Oswald. Substrate temperature changes during molecular beam epitaxy growth of gamnas. *Journal of Applied Physics*, 102(8):083536, 2007.

[35] Gaussovské svazky. `https://physics.mff.cuni.cz/kchfo/ooe/pdf/praktika_gauss.pdf`.

[36] Charlotte Bond, Daniel Brown, Andreas Freise, and Kenneth A. Strain. Interferometer techniques for gravitational-wave detection. *Living Reviews in Relativity*, 19(1), December 2016.

[37] The measurement of a transverse profile of laser beam by knife edge method. `https://people.fjfi.cvut.cz/blazejos/public/ul7en.pdf`.

List of Figures

List of Tables